
Electronic Thesis and Dissertation Repository

10-23-2017 2:00 PM

Characterization of an Orthotopic Rat Model of Glioblastoma Using Multiparametric Magnetic Resonance Imaging and Bioluminescence Imaging

Trung Le, *The University of Western Ontario*

Supervisor: Scholl, Timothy J., *The University of Western Ontario*

Joint Supervisor: Ronald, John A., *The University of Western Ontario*

A thesis submitted in partial fulfillment of the requirements for the Master of Science degree in Medical Biophysics

© Trung Le 2017

Follow this and additional works at: <https://ir.lib.uwo.ca/etd>



Part of the [Medical Biophysics Commons](#)

Recommended Citation

Le, Trung, "Characterization of an Orthotopic Rat Model of Glioblastoma Using Multiparametric Magnetic Resonance Imaging and Bioluminescence Imaging" (2017). *Electronic Thesis and Dissertation Repository*. 5057.

<https://ir.lib.uwo.ca/etd/5057>

This Dissertation/Thesis is brought to you for free and open access by Scholarship@Western. It has been accepted for inclusion in Electronic Thesis and Dissertation Repository by an authorized administrator of Scholarship@Western. For more information, please contact wlsadmin@uwo.ca.

Abstract

Glioblastoma multiforme (GBM) is a lethal and nearly incurable disease. The C6 rat model of GBM shares several similarities to human GBM and longitudinal imaging may allow tumour features to be studied. In this thesis, a multimodality imaging framework, consisting of bioluminescence imaging (BLI) and multiparametric magnetic resonance imaging (mpMRI), was applied to the C6 rat model to characterize the growth of orthotopic tumours. BLI signal, a measure of cell viability, tended to increase and then decrease in most of animals, whereas tumour volume (from MRI) continually increased. Cellular viability and tumour volume did not correlate across all days, highlighting the value of using complementary imaging modalities. Apparent diffusion coefficient maps and immunohistochemistry suggests that decreases in BLI signal are, in part, due to decreased tumour cellularity (*i.e.* necrosis). This is the first use of BLI and mpMRI to characterize this model, and highlights the inter-subject variability in tumour growth.

Keywords

glioblastoma multiforme, C6 rat model, bioluminescence imaging, multiparametric magnetic resonance imaging, diffusion-weighted imaging, immunohistochemistry

Co-Authorship Statement

This thesis contains materials that will be submitted for a publication and contains materials that have previously been presented at various conferences. The contributions of the co-authors are discussed below.

The manuscript (chapter 2) will be submitted to the journal *Tomography* for publication. The co-authors of this manuscript are Heeseung Lim, Amanda M. Hamilton, Katie M. Parkins, Yuanxin Chen, Timothy J. Scholl, and John A. Ronald. As the first author of the manuscript, I made significant contributions to this project and I was responsible for many aspects of this thesis, research and manuscript preparation. I was responsible for the collection of the data during the experiments, as well as the interpretation and analysis of the results. I was responsible for the preparation all text and the creation of the figures. Heeseung Lim helped in the collection of MRI data and the analysis of the data presented in this thesis. Amanda M. Hamilton was responsible for genetically engineering the C6 glioma cells to express *Luciola Italica* luciferase. Yuanxin Chen aided in immunohistochemistry and the staining and scanning of histological sections. Drs. Timothy J. Scholl and John A. Ronald, my supervisors, were responsible for overseeing of all my research and provided feedback on the interpretation of the results. They were responsible for the general research framework and provided the main ideas and necessary tools to conduct the research. All authors were involved in the editing and revision of the manuscript.

Acknowledgments

Firstly, I would like to thank my supervisors and mentors, Drs. Timothy J. Scholl and John A. Ronald, for constantly providing me guidance during my Master's degree. They always provided motivation and pushed me to achieve greater goals. They have both provided me with endless opportunities to grow and learn. Thank you for being an amazing supervisor, a mentor and friend.

I would like to thank my lab mates Nolan, Nivin, Ali, Yonathan, Katie, Patrick, Richard, Amanda, and Paco for always providing me with support when I had endless questions. You are all amazing people, and are all filled with amazing personalities. I appreciate all of your patience while helping and guiding me during my Master's degree. I will always cherish the memories we've created together.

A special thanks to the cat people, Dave and Matt, who provided insight to this research and provided lots of joyful memories. Lewis, Dindy and Dolce, thank you for all of your support.

Special thanks to my loving significant other and cat, Tiffany and Milo. Thank you for always being there for me when I needed you the most. I appreciate all the support you both have given me to achieve greater goals and to help bring them to fruition. Thank you for always being by my side.

Table of Contents

Abstract.....	i
Co-Authorship Statement.....	ii
Acknowledgments.....	iii
Table of Contents.....	iv
List of Figures.....	vi
List of Abbreviations.....	vii
General Introduction.....	1
1.1 Cancer and Brain Cancer (Glioma).....	1
1.2 Glioblastoma Multiforme (GBM).....	2
1.2.1 Treatment of GBM.....	3
1.3 Clinical Imaging of GBM.....	3
1.3.1 MRI Diagnosis and Monitoring of GBM.....	4
1.3.2 The Macdonald Criteria.....	5
1.3.3 Response Assessment in Neuro-Oncology (RANO) Criteria.....	7
1.4 Preclinical GBM Models.....	11
1.4.1 C6 GBM Rat Model.....	13
1.5 Imaging of the C6 GBM Rat Model.....	15
1.6 MRI and Multiparametric MRI (mpMRI) in the C6 Rat GBM Model.....	16
1.6.1 T ₁ -, T ₂ -, Post-Gd T ₁ -weighted and Diffusion MRI.....	22
1.7 Bioluminescence Imaging.....	24
1.8 Thesis Overview.....	29
1.9 References.....	31
Chapter 2.....	39
2 Multiparametric Magnetic Resonance Imaging and Bioluminescence Imaging Characterization of an Orthotopic Rat Model of Glioblastoma.....	39

2.1	Introduction.....	39
2.2	Methods and Materials.....	42
2.2.1	Cells	42
2.2.2	Lentiviral Transduction.....	43
2.2.3	In Vitro Cell Analysis	45
2.2.4	Orthotopic C6 Glioma Rat Model.....	46
2.2.5	Bioluminescence Imaging (BLI).....	46
2.2.6	Multiparametric Magnetic Resonance Imaging (mpMRI)	47
2.2.7	Image Analysis.....	48
2.2.8	End-Point Histology.....	49
2.2.9	Statistics	49
2.3	Results.....	50
2.4	Discussion.....	63
2.5	References.....	71
	General Discussion and Conclusions.....	76
3	Overview	76
3.1	Summary and Conclusions	76
3.2	Limitations	78
3.3	Future Directions	80
3.4	Significance and Impact.....	82
3.5	References.....	82
	Appendix.....	84
	Appendix A. Animal Research Ethics Approval	84
	Curriculum Vitae	88

List of Figures

Figure 1-1. Bioluminescence chemical reaction equation.	27
Figure 2-1. Lentiviral Engineering of C6 Glioma Cells with Reporter Genes.	44
Figure 2-2. In vitro analysis of luciferase expression versus cell numbers, doubling rate, and luciferase activity over passage number.	51
Figure 2-3. BLI of C6Luc orthotopic tumour growth in Wistar rats.	53
Figure 2-4. Representative longitudinal post-Gd T ₁ - and T ₂ -weighted MRI of C6Luc tumour growth.	55
Figure 2-5. Correlational plots of total T ₂ and post-Gd T ₁ tumour volume to BLI signal.....	57
Figure 2-6. Longitudinal post-Gd T ₁ -weighted MRI with CE and NCE regions differentiated and examined for correlation.	59
Figure 2-7. Longitudinal apparent diffusion coefficient (ADC) maps and post-Gd T ₁ -weighted MRI with their respective plots.	60
Figure 2-8. Fully co-registered whole brain histology, which includes H&E, DAPI, GFP and hypoxia, to post-Gd T ₁ -weighted MR images with the respective co-registered ADC maps of four representative animals.	62

List of Abbreviations

¹⁸ F-galacto-RGD	¹⁸ F-galacto-arginine-glycine-aspartic acid
2D	two-dimensional
3D	three-dimensional
ADC	apparent diffusion coefficient
AMP	adenosine monophosphate
ATP	adenosine triphosphate
B ₀	main magnetic field
B ₁	radiofrequency pulse
BBB	blood-brain barrier
BLI	bioluminescence imaging
BRAVO	brain volume imaging
BTB	blood-tumour barrier
C6Luc150	luciferase expressing C6 cells with 150 µg/mL D-luciferin
CCD	charge-coupled device
CE	contrast enhanced
CO ₂	carbon dioxide
CSF	cerebral spinal fluid
CT	computed tomography
DAPI	4',6-diamidino-2-phenylindole
DBT	dihydrolipoamide branched chain transacylase E2
DCE	dynamic contrast enhanced
D-Luc	D-luciferin
DTI	diffusion tensor imaging
DTPA	diethylenetriaminepentacetate
DWI	diffusion-weighted imaging
EGFR	epidermal growth factor receptor
ETL	echo train length
FACS	fluorescence-activated cell sorting
FDG	¹⁸ F-fluorodeoxy-D-glucose
FET	¹⁸ F-fluoro-ethyl-L-tyrosine
FID	free induction decay
FLAIR	fluid-attenuated inversion recovery
FLuc	firefly luciferase
FMISO	¹⁸ F-fluoromisonidazole
FOV	field of view
GBM	glioblastoma multiforme
Gd	gadolinium
GEM	genetically engineered mice

GFP	green fluorescent protein
GRE	gradient recalled echo
G_x	gradient field in the x Cartesian direction
G_y	gradient field in the y Cartesian direction
G_z	gradient field in the z Cartesian direction
H&E	hematoxylin and eosin
HBSS	Hank's buffered salt solution
Her3	human epidermal growth factor receptor 3
HP	hyperpolarized
IGF-1	Insulin-like growth factor 1
Luc	<i>Luciola Italica</i> luciferase
Mg	magnesium
MOI	multiplicity of infection
mpMRI	multiparametric magnetic resonance imaging
MRI	magnetic resonance imaging
MRS	magnetic resonance spectroscopy
MRSI	magnetic resonance spectroscopic imaging
NCE	non-contrast enhanced
NEX	number of averages
Non-CE	non-contrast enhancement
O_2	oxygen
PDGF β	platelet-derived growth factor-beta
PDX	patient derived xenograft
PET	positron emission tomography
PFA	paraformaldehyde
PWI	perfusion weighted imaging
RANO	response assessment in neuro-oncology
RF	radiofrequency
RLuc	renilla luciferase
ROI	region of interest
SE	spin echo
SNR	signal-to-noise ratio
SPECT	single-photon emission tomography
T_1	longitudinal relaxation time
T_2	irreversible transverse relaxation time
T_2^*	total transverse relaxation time
TE	echo time
TR	repetition time
WHO	world health organization

General Introduction

1.1 Cancer and Brain Cancer (Glioma)

Cancer is the leading cause of death in Canada and is responsible for approximately 30% of all deaths. It is estimated that 1 in 2 Canadians will develop some form of cancer in their lifetime, and an estimated 1 in 123 Canadians will develop brain cancer (1). Glioma is the most common form of malignant primary brain tumours and arises *de novo* from glial cells in the brain (2). Unfortunately, glioma is the leading cause of cancer-related death in children, adolescents, and young adults, being responsible for approximately 26% of mortality among cancer patients (1).

Gliomas are classified based on morphological appearance and World Health Organization (WHO) grades. Since gliomas do not necessarily resemble the glial cells they originated from, they are categorized based on morphological appearance. Generally, gliomas may resemble astrocytes, oligodendrocytes, or ependymal cells and are thus referred to as astrocytomas, oligodendrogliomas, or ependymomas, respectively (3). In addition, the WHO grades glioma into four groups based on histopathological features and malignancy (4). Grade I gliomas, which are the least malignant, are lesions with minimal proliferative potential and can be cured through surgical resection alone. Grade II gliomas are infiltrative neoplasms that frequently recur despite the low proliferative potential and have the potential to progress to higher malignancy grades. Tumours are categorized as grade III when lesions have histological evidence of nuclear atypia and increased mitotic activity. Grade IV tumours, specifically glioblastoma multiforme (GBM), are highly aggressive,

malignant, invasive, proliferative and tend to develop necrotic foci, all of which are associated with rapid disease evolution and extremely poor prognosis (4).

1.2 Glioblastoma Multiforme (GBM)

The most invasive and lethal primary brain tumour is a glioblastoma multiforme (GBM), which accounts for approximately 50% of all glioma cases (2). GBM is considered as a WHO grade IV astrocytoma and generally develops *de novo*, meaning these tumours can develop spontaneously within the brain and does not arise from the migration of another tumour found within the body (5). The 5-year relative survival rate, which is an estimated measure for the probability of a patient surviving 5 years after diagnosis, for ages 20-44, 45-54 and above 55 is 14%, 4% and less than 1%, respectively (1). GBM is characterized by its infiltrative growth, which makes differentiation between tumour tissue and normal tissue nearly impossible in some cases, as well as its tendency to develop necrotic foci and its ability to aggressively proliferate (5). There are two main necrotic formations described by Urbanska *et al.*; one is large areas of necrosis near the centre of the tumour due to the lack of blood supply and the second is smaller irregularly shaped necrotic areas throughout the tumour. As the name suggests, GBM may contain heterogenous cellular features and anaplastic cells, which can contribute to its severity and resistance to conventional therapy (6). Despite aggressive treatment regimens, as described more extensively below, the median survival time for patients after diagnosis of GBM is 12-15 months (4).

1.2.1 Treatment of GBM

The standard treatment of GBM consists of complete surgical resection when possible, followed by radiotherapy and temozolomide chemotherapy (7). However, this treatment regimen almost always fails, in part due to the aggressive and infiltrative nature of this disease (8). In addition, maximal surgical resection is not always possible due to the inability to distinguish tumour from normal tissue, or the tumour's location near essential brain regions, and as a result, surgical resection may be inefficient (9). In addition, chemotherapeutic efficacy may be further reduced due to the blood-brain barrier or regions of poor vasculature within the tumour (10).

With the lack of effective treatment regimens available for patients, novel therapies have been investigated such as; anti-angiogenic gene therapy to combat the rapid vascularization of GBM (11), immunotherapy to increase survivorship (12), and hormone therapy to inhibit GBM growth and to induce apoptotic pathways (13). The ability to image, monitor and evaluate the tumour during treatment plays a key role in better assessing, understanding and treating this disease.

1.3 Clinical Imaging of GBM

The ability to non-invasively measure and evaluate tumour progression will aid in the diagnosis and control of GBM because the ability to detect these tumours sooner can improve patient survivorship by beginning treatment before the tumour becomes too large and infiltrative. In addition, evaluation of tumour response to therapy will aid in the treatment of this disease because ineffective treatments may be identified sooner and

salvage treatment can begin, maximizing patient survivorship. The standard imaging techniques used to diagnose and monitor patients with brain tumours are X-ray computed tomography (CT), otherwise known as a computerized axial tomography scan, and magnetic resonance imaging (MRI). CT scans are the standard for patients that are ineligible for MRI, *e.g.* patients with pacemakers (14-16). MRI provides high-resolution imaging with excellent soft tissue contrast, and unlike CT, does not require the use of ionizing radiation. The availability of different pulse sequences to yield varying endogenous contrast, in addition to the use of exogenous contrast agents, increases the effectiveness of MRI to diagnose GBM, as well as obtain information about various anatomical and functional characteristics within a GBM (16). For example, standard anatomical imaging includes 2D or 3D pre-contrast T_1 - and T_2 -weighted, fluid-attenuated inversion recovery (FLAIR), and post-gadolinium-diethylenetriaminepentaacetate (Gd-DTPA) T_1 -weighted images. Several other imaging modalities or techniques have been used to evaluate biological, functional and molecular features of GBM such as magnetic resonance spectroscopy (17), blood oxygen level-dependent MRI (18), diffusion weighted MRI (19), and perfusion MRI (20). In addition to MRI and CT, nuclear medicine techniques such as positron emission tomography (PET)(21), and single-photon emission computed tomography (SPECT)(22, 23) have also been used to monitor and evaluate GBM progression.

1.3.1 MRI Diagnosis and Monitoring of GBM

MRI plays a key role in the diagnosis and treatment assessment of GBM. Patients will undergo neurological exams and initial diagnostic imaging sessions if GBM is suspected. Once GBM is confirmed by the neurologist, a biopsy, through surgical resection or fine

needle aspiration, is performed to obtain tissue for pathological diagnosis (24, 25). Once the tumour has been assessed, graded, and therapy has been planned, the patient will undergo several additional MR imaging sessions. MRI serves as the standard to monitor and evaluate tumour response to therapy over a period of weeks. MRI also provides important information during treatment planning, *e.g.* planning the maximum safe margin for surgical resection.

1.3.2 The Macdonald Criteria

The former standard for evaluating tumour progression and response was established by the Macdonald criteria. These criteria are predominantly dependent on anatomical changes, which may be changes in tumour enhancement on consecutive post-Gd T_1 -weighted MRI scans obtained at least one month apart.

The tumour is assessed for changes based on the size of the largest cross-sectional area of the enhancing tumour on post-Gd T_1 -weighted MRI. The size of the enhancing tumour is measured by taking the product of two perpendicular maximal diameters on a two-dimensional post-Gd T_1 -weighted MR image (26). In addition, the Macdonald criteria also include neurological assessments and changes in steroid use when assessing treatment response. Treatment response can be categorized into four groups: complete response, partial response, progressive disease and stable disease.

Complete response occurs when there is a disappearance of enhancing tumour on consecutive post-Gd T_1 -weighted MRI at least one month apart and patient neurological function and behaviour improves without the use of steroids. Partial response occurs if there is a greater than 50% reduction, relative to baseline, in enhancing tumour size over

consecutive post-Gd T_1 -weighted MRI scans at least one month apart, with no new lesions. Neurological behaviour must be clinically stable or improved and the patient must be on a stable or reduced dose of steroids. Progressive disease occurs if the size of enhancing tumour increases by more than 25% on consecutive post-Gd T_1 -weighted MRI scans at least one month apart, with the appearance of new lesions or clinical deterioration. Stable disease occurs if the patient does not meet the required changes in enhancing tumour size, neurological function or steroid use. Thus, the patient cannot be categorized as complete response, partial response or progressive disease, *i.e.*, every other remaining situation (16, 26, 27).

The Macdonald criteria have proven to be extremely useful in the clinical assessment of glioma response to therapy. However, there are several limitations including the difficulty to measure irregularly-shaped GBMs and enhancing lesions in the cystic or surgical cavity (because the cavity itself may be included in the measurement of tumour size), interobserver variability and lack of criteria for measuring non-enhancing components of the tumour on post-Gd T_1 -weighted MR images and multifocal tumours (28). One severe limitation associated with the Macdonald criteria is that contrast enhancement from Gd-DTPA is non-specific and primarily reflects the passage of contrast agent across a disrupted blood-brain barrier. This enhancement may be influenced by other factors such as dose of steroids, anti-angiogenic therapy, inflammation, ischemia, post-surgical change, and radiation necrosis. Thus, these tumours may be subject to a phenomenon known as pseudoprogression or pseudoresponse. Pseudoprogression refers to a temporary increase in enhancement size in post-Gd T_1 -weighted MRI post-treatment when compared to baseline MR images. This may cause the misdiagnosis of the tumour to be categorized as

progressive disease, when in fact these changes are transient and not reflective of the true nature and size of the tumour. These changes may be associated with an increased permeability to contrast agent following radiotherapy and chemotherapy and may ultimately lead to premature discontinuation of adjuvant therapy. On the contrary, pseudoresponse refers to a temporary decrease in enhancement size in post-Gd T_1 -weighted MR images post-treatment when compared to baseline MR images. Like pseudoprogession, these changes are transient and may cause the incorrect clinical assessment of a non-responding tumour, ultimately leading to several weeks of ineffective therapy (28).

A newer method of treatment assessment, which has largely superseded the Macdonald criteria, is referred to as the Response Assessment in Neuro-Oncology (RANO) criteria and has been developed to address the drawbacks and limitations associated with the Macdonald criteria by introducing several additional measurements encompassing a wider range of factors to increase clinical assessment reliability (15, 20).

1.3.3 Response Assessment in Neuro-Oncology (RANO) Criteria

The current gold standard for clinically assessing GBM response to treatment is the RANO criteria. It largely builds upon the foundation of the Macdonald criteria, while adding additional measurements and standardizing imaging definitions. The RANO criteria utilizes T_2 , FLAIR, and post-Gd T_1 MR images to accurately and reliably assess treatment response when compared to the Macdonald criteria. T_2 -weighted MRI provides contrast of the tumour without the use of contrast agent, while FLAIR MRI provides similar contrast to T_2 -weighted MRI but suppresses signal from fluids such as the cerebral spinal fluid

(CSF). Post-Gd T_1 -weighted MRI provides signal enhancement of tumour tissue but requires the delivery of Gd-DTPA to tumour tissue. The RANO criteria incorporate measurements of multifocal tumours and enhancing and non-enhancing lesions using the product of the maximal cross-sectional diameter as used in the Macdonald criteria. Where enhancing and non-enhancing lesions refer to lesions seen on post-Gd T_1 -weighted and FLAIR/ T_2 -weighted MRI, respectively. In addition, the RANO criteria make an important distinction between measurable and non-measurable disease detected using contrast enhancement. Where measurable disease refers to tumours with a minimal size both in and out of plane, have contrast enhancement on post-Gd T_1 -weighted MRI and do not include the cavity, cyst or necrosis. Non-measurable disease refers to lesions that are too small, do not enhance (in other words seen only in T_2 /FLAIR MRI) or have poorly defined margins.

The RANO criteria assert that a lesion is considered measurable when there is bi-dimensional contrast enhancement with clear tumour margins in post-Gd T_1 -weighted MRI with a minimal size requirement of 10 mm if the slice thickness is less than 5 mm and two times the slice thickness if the slice thickness of the image is larger than 5 mm. It also specifically states that any cystic or surgical cavity should not be measured unless there is a measurable lesion at least 10 mm in diameter. Non-measurable lesions generally do not meet the requirements above. They are defined as unidimensional lesions, tumour masses without a clear defined margin or lesions not greater than 10 mm in the maximal perpendicular diameter.

Patients without measurable lesions cannot be categorized as responders to treatment and can only achieve stable disease. The RANO criteria consider multiple contrast-enhancing lesions, and a minimum of two to five lesions will be measured to determine the size of the

tumour, which will be used to assess treatment response. However, the RANO criteria emphasize reproducibility and accuracy of measurements; therefore, multifocal lesions with large measurement uncertainties may be omitted and the next best lesion may be measured.

The RANO criteria also address the large issue of pseudoprogression during the first 12 weeks of chemoradiotherapy. Thus, progression is only defined when there is tumour enhancement outside the radiation field in post-Gd T_1 -weighted MRI, or if there is histological evidence of large tumour areas. Beyond 12 weeks, disease progression is deemed to occur when; 1) there are new contrast-enhancing lesions outside of the radiation field regardless of steroid use, 2) if there is a greater than 25% increase in tumour size from the first post-radiotherapy scan to subsequent scans 12 weeks later with increased or maintained steroid use, 3) clinical deterioration not associated with therapy occurs, and 4) there is a significant increase in T_2 -weighted or FLAIR non-enhancing lesions in patients undergoing antiangiogenic therapy.

Within this assessment framework, the RANO criteria categorize treatment response into four groups; complete response, partial response, stable disease or progression. Complete response occurs when there is a disappearance of all enhancing and non-measurable disease over a period of at least 4 weeks. Non-enhancing lesions evident after T_2 -weighted or FLAIR MRI are those that have stabilized or reduced in size and the use of steroids are stable or reduced from baseline. Partial response is defined by a greater-than-50% size reduction in all measurable enhancing lesions, no progression of non-measurable disease, no new lesions, stable or improved lesions on T_2 or FLAIR MRI, and stable or lower steroid usage between scans at least four weeks apart. Stable disease is defined by tumours that do

not meet all the criteria for the other treatment response groups, but where there are no new T_2 or FLAIR lesions on the same or lower steroid dose when comparing the baseline scan to the post-treatment scan. Progression occurs if any of the following occur; 1) the sum of perpendicular diameters of enhancing lesions increase by more than 25% on stable or higher steroid doses, 2) there is a significant increase in T_2 or FLAIR non-enhancing lesions, 3) new lesions appear, or there is clear progression of non-measurable lesions or clear-clinical deterioration of the patient's health (27, 28).

The Macdonald criteria predominantly relied on changes in tumour size based on post-Gd T_1 -weighted MRI, patient neurological behavior and corticosteroid use, to assess treatment response without considering other imaging contrast techniques, irregular shaped and multifocal tumours. On the other hand, the RANO criteria places emphasis on measuring lesions on multiple imaging contrast techniques such as, FLAIR, T_2 , post-Gd T_1 -weighted MRI. The RANO criteria applies stricter guidelines to measure tumours and categorize a patient as responsive or progressive, such as including chemoradiotherapy timing, corticosteroid use, type of treatment applied, measuring multifocal tumours, measuring non-enhancing lesions and considering lesions as measurable or non-measurable based on anatomical features. The RANO criteria are continually evolving to consider modern advances in neuroimaging and discoveries related to GBM biology. Although the RANO criteria have updated and improved the foundations set by the Macdonald criteria, significant limitations are still apparent such as the lack of implementation of volumetric information and the minimum time requirement between scans required for assessing treatment response.

1.4 Preclinical GBM Models

Preclinical animal models are extremely useful to allow researchers to better understand tumour biology and disease progression, and to test novel therapeutics prior to their translation into patients. Animal models, such as rodents, are important tools in experiments because they are easy to handle, have a short life span, and develop a central nervous system similar to that of humans. Novel imaging techniques may be developed to address clinically-relevant issues such as the lack of accurate and reliable metrics to measure tumour response to therapy. For instance, imaging techniques such as anatomical MRI and diffusion-weighted imaging (DWI) have been applied to assess the effects of novel therapies in these models (19, 29).

Various animal models have been developed that recapitulate features seen in human GBM such as; 1) a similar genetic background, 2) intratumoral heterogeneity that includes genetic, epigenetic or phenotypic changes, 3) similar microenvironmental features such as the presence of the blood-brain barrier (BBB), cellular interactions, immunological responses, and 4) stability and reproducibility (30). There are currently many murine GBM cell lines used to mimic human GBM once they've been implanted into the brains or bodies of mice, such as the U251, U87, and GL261 cell lines. Each species-specific model has its own particular limitations and advantages, and each glioma model provides varying similarities to human GBM but may have several other applications (31). For example, the U251 glioma model shares several histological and immunohistochemically features of human GBM, genetic alterations and imaging features, such as necrosis. The U87 model has several dissimilarities to the U251 and human GBM, but proves an excellent model to

assess angiogenesis and anti-angiogenesis therapy (32). The previous two models rely on immune incompetent mice, while the GL261 syngeneic model does not. Thus, GL261 orthotopic homografts may experience an immunological response that is typically found in patients, and thus tumour progression may closely mimic human GBM progression (31). This is a particularly strong model for evaluating immune-based therapies (31). In addition, patient-derived xenograft (PDX) GBM models is an attractive alternative. These tumours are obtained from patients and are directly implanted into animals and are based on the assumption that these models faithfully resemble the original tumours.

However, detailed imaging of the mouse brain may be limited due to the inherently small size of the brain. The ability to visualize intratumoural features may be limited due to limited spatial resolution and signal-to-noise ratio (SNR) of some imaging modalities (33). To address this limitation, state-of-the-art MRI hardware is required specifically for small animal imaging, which may be costly and available at a few imaging centres all over the world. Thus, an alternative animal host, such as rats, may be used to study GBM.

Rat models using rat glioblastoma cell lines such as the C6, 9L, CNS-1 or F98 have proven to be useful to probe tumour biology and progression in the brain (31, 34). The 9L rat glioblastoma model has been extensively used to study chemotherapy or radiotherapy regimens (34), and has served as a useful model to better understanding human GBM. However, the 9L is considered a gliosarcoma, which is a subset of grade IV gliomas (34). Therefore, this model may not represent human GBM reliably and accurately, and one of its greatest limitations is that it does not show the diffuse infiltrative growth found in human GBM (31). The CNS-1 model is a relatively newer relative to the C6 and 9L rat models and thus lacks extensive literature reporting the genetics and biology of the model.

However, it shares several histological markers and growth patterns with human GBM and serves as an excellent model to understand human GBM (31). The F98 glioma model shares several characteristics, such as increased expression of cancer genes and/or proteins, to human GBM and C6 cells. This model expresses highly invasive growth patterns with fairly low immunogenicity, making it an attractive model to evaluate therapeutic agents and to better study the mechanisms underlying glioma resistance to immunotherapy. The F98 model has also been genetically engineered to express the BLI reporter gene, luciferase, to monitor tumour size (34). The C6 model, which was used in this project, is described more fully in the next section.

1.4.1 C6 GBM Rat Model

The C6 cell line was first developed by Benda *et al.* (35) and Schimdek *et al.* (36) in the 1960's by repetitively administering a carcinogen known as N-Nitroso-N-methylurea over a period of 8 months into outbred Wistar rats. The C6 GBM rat model was first described by Auer *et al.* (37), and it is an intracranial brain tumour model used to study GBM experimentally. The model was developed by injecting 1 to 5×10^5 C6 cells into the brains of rats. These tumours developed similar morphologically features to human GBM and became a popular animal model to study the progression and treatment of human GBM. Since its development, the pathological, molecular, and genomic characteristics of the C6 model have been extensively characterized (8, 37-40). This model shares several histopathological and specific tumour markers with human GBM such as diffuse infiltrative growth patterns (31), nuclear pleomorphism, high mitotic activity, regions of necrosis within the tumour, hemorrhage, and parenchymal invasion (40). Recent molecular

characterization of this cell line has shown several changes in gene expression reported in human tumours (38).

The C6 cell line is reported to have mutations in the p16/Cdkn2a/Ink4a locus (39), which is commonly associated with tumour suppression and often mutated in human GBM. However, the C6 has a wildtype tumour suppressor gene, p53, (41) unlike human GBM. When compared to astrocytes, the C6 cell line has increased gene expression of platelet-derived growth factor-beta (PDGF β), insulin-like growth factor 1 (IGF-1), epidermal growth factor receptor (EGFR), and human epidermal growth factor receptor 3 (Her3) genes, which are commonly overexpressed in human gliomas (34). C6 cells have increased activity of the *Ras* pathway also seen in human GBM and contrary to what has been reported for human GBM, C6 cells have an increased expression of retinoblastoma protein (34).

The study of the C6 rat model has contributed to the clinical understanding of GBM and its treatment, which includes the extent of tumour progression, the potential for spontaneous regression, the patterns of cell infiltration and neoangiogenesis (42). This model has been extensively used in various experimental neuro-oncology studies using novel treatment modalities such as anti-angiogenic therapy (43), cytotoxic gene therapy (44), and treatment with toxins (45). In addition, this model has found an extensive use to evaluate the efficacy of immunotherapy because the C6 cell line was found to be immunogenic in all rats including the Wistar rat, which the model was derived (34). Evaluating immunotherapy in an immune competent animal capable of exhibiting an immune response is beneficial because it closely mimics the biology and immune response seen in of human GBM.

Advances in modern non-invasive neuroimaging techniques and modalities has provided an opportunity to better understand and study GBM. The imaging of this model will be further discussed in the next section.

1.5 Imaging of the C6 GBM Rat Model

The ability to non-invasively image GBMs *in vivo* has provided a great deal of information regarding the formation and development of such tumours. Advances in modern neuroimaging techniques have improved the characterization of physiology and metabolism of GBM which may lead to improved clinical assessments and outcomes (46). The identification and pursuit of potential biomarkers for imaging in GBM may provide new opportunities to better treat and understand this disease.

Many imaging modalities and techniques have been applied to the C6 rat model and reported in the literature. Some examples include; standard anatomical imaging used in patients such as pre-contrast T_1 -weighted and T_2 -weighted MRI, FLAIR MRI, post-Gd T_1 -weighted MRI (42), and CT (47). In addition, relatively newer MR techniques have been explored including DWI (48), diffusion tensor imaging (DTI)(49), perfusion-weighted imaging (PWI)(50), proton (^1H) magnetic resonance spectroscopy (MRS)(51), and hyperpolarized (HP) ^{13}C magnetic resonance spectroscopic imaging (MRSI)(52). The C6 rodent model has also been imaged using various PET tracers such as ^{18}F -fluorodeoxy-D-glucose (FDG)(53) to probe glucose metabolism within the tumour, ^{18}F -fluoro-ethyl-L-tyrosine (FET)(54) to delineate tumour tissue from healthy tissue and to aid in the identification of malignant tissue, ^{18}F -fluoromisonidazole (FMISO)(55) which identifies regions of hypoxia, perfusion CT (56), and ^{123}I -iodo-L- α -methyltyrosine SPECT (57).

Preclinical models are amenable for the use of imaging modalities because novel imaging modalities or techniques may be used and can offer additional advantages at a lower cost. For instance, BLI, discussed more fully below, can provide direct measures of relative cellular viability over time, which is a measurement of live cells based on enzymatic activity and light production. Literature description of the use of BLI with the C6 cell line is relatively sparse. For example, Yeom *et al.* visualized hypoxia-inducible-factor-1 in xenograft mice models using BLI (58). Jang *et al.* explored the use of BLI to monitor the therapeutic efficacy of a novel treatment in a C6 mouse model (59). To date, Xi *et al.* has been the only group to apply BLI to a C6 rat model. They used BLI to longitudinally monitor the efficacy of two novel therapies in a brainstem xenograft C6 rat model (60, 61). Novel therapies may be evaluated using a combination of these imaging modalities to provide significantly more information than the use of a single imaging technique.

1.6 MRI and Multiparametric MRI (mpMRI) in the C6 Rat

GBM Model

Magnetic resonance imaging (MRI) is a non-invasive *in vivo* imaging modality capable of obtaining both anatomical and functional information within the body. MRI involves the interaction of a nucleus (*e.g.* ^1H) in a molecule within tissue with an applied external magnetic field. MRI utilizes large static magnetic fields from superconductive magnets, rapidly manipulated magnetic field gradients from resistive magnets, and radiofrequency (RF) excitation and reception to generate images based on intrinsic physical properties of the nuclei. These include nuclear spin, gyromagnetic ratio, abundance, spin-spin (T_2) and spin-lattice (T_1) relaxation values.

The usual nuclei imaged in conventional MRI is the ubiquitous proton (^1H) associated with the water molecule. Intrinsic properties such as $\frac{1}{2}$ -nuclear spin, large gyromagnetic ratio, and high concentration in tissue make it the most useful nucleus for *in vivo* MRI. The nuclear spin angular momentum, colloquially known as “spin”, is a quantum mechanical property. Nuclei can possess only integer or half-integer spin and spin- $\frac{1}{2}$ nuclei are the most useful for MRI due to the manner in which they interact with electric and magnetic fields they experience within their environment. These interactions govern properties such as spin-lattice and spin-spin relaxation. The strength of interaction of a nucleus with an applied magnetic field is proportional to its nuclear magnetic dipole moment. The gyromagnetic ratio is the ratio of a particle’s magnetic dipole moment to its spin angular momentum. Therefore, a nucleus with a larger magnetic moment (and thus a larger gyromagnetic ratio) will interact more strongly with an external field and produce more signal for MRI. MR anatomical imaging is possible due to these favourable intrinsic properties of protons and their large abundance (in the form of water) within the body. This facilitates high-resolution three-dimensional imaging with excellent soft tissue contrast.

A typical MRI instrument consists of three distinct electromagnetic systems; the main magnetic field, the gradient fields, and the RF transmit/receive system. A system of superconducting magnet windings creates the strong main magnetic environment (B_0) required for magnetization of the protons within water molecules. In the absence of an external magnetic field, the magnetic dipole moments of nuclei are randomly oriented. However, when protons are exposed to an external magnetic field, they begin to precess around the field direction. For an ensemble of magnetic dipoles, the angles of the precessional cone are nearly randomly distributed with respect to the magnetic field

direction but are slightly skewed in the direction of the field. This produces a weak net “magnetization” along the magnetic field direction. It is this “longitudinal” magnetization, that is the source of the signal for MRI. The amount of magnetization depends on the magnetic field strength, the gyromagnetic ratio of the nucleus and its abundance in the body.

The gradient coil system consists of layers of resistive magnet windings wound on a cylindrical form located inside the superconducting magnetic field, B_0 . These gradient magnets superimpose a linear spatial change in the homogenous main magnetic field in three orthogonal directions, G_x , G_y and G_z . These linear gradients are independently manipulated with great speed to alter the frequency and phase of the precessing nuclei within the main magnetic field. Systematic control of this motion is known as frequency and phase encoding, which is used to “encode” the MRI signal with spatial information so that three-dimensional imaging data can be acquired.

The RF coil is located within the gradient structure. Its purpose is to transmit the RF energy (B_1) required to excite the magnetization of the protons of water molecules present in tissue and to detect its subsequent electromagnetic signal, which is used to produce an image. The B_1 magnetic field is oriented orthogonally to the main magnetic field and oscillates (or rotates) at the nuclear precession frequency. This is known as the Larmor frequency, which is equal to the product of the nuclear gyromagnetic ratio multiplied by the magnetic field strength. The B_1 field causes a portion of the longitudinal magnetization of the protons to be excited (or tipped) into the plane orthogonal (*i.e.* transverse) to the main magnetic field. The resulting “transverse magnetization” precesses around B_0 at the Larmor frequency, as its amplitude decays with an exponential time constant, T_2 , known as the spin-spin

relaxation constant. Spin-spin relaxation is an intrinsic tissue property. For example, the T_2 relaxation times of CSF and fat at the clinical field strength of 3 Tesla (T) are approximately 2000 ms and 70 ms, respectively (62). This difference in spin-spin relaxation time for various tissues can be exploited to produce image contrast for MRI known as T_2 -weighted imaging and can be used to differentiate morphology based on tissue type. In addition, during the loss of transverse magnetization, the longitudinal magnetization recovers asymptotically to its equilibrium along B_0 . This is known as spin-lattice relaxation and is characterized by the exponential time constant, T_1 . As with T_2 relaxation times, T_1 relaxation times are tissue specific. For example, the T_1 relaxation times for CSF and fat at 3 T are 4000 ms and 250 ms, respectively (62). Again, this intrinsic magnetic property of the protons in tissues can also be used to produce an endogenous image contrast known as T_1 -weighted contrast. In addition to T_1 - and T_2 -weighted contrast other imaging contrasts can be generated such as proton density contrast and diffusion-weighted images.

Extrinsic parameters such as repetition time (TR) and echo time (TE) influence the manipulation of the proton magnetization during image acquisition, which in turn affects imaging contrast and SNR. The repetition time refers to the time between RF excitation pulses. The echo time refers to the time between the initial RF pulse excitation and the centre of the signal echo used to refocus (or recycle) the transverse magnetization. These are key timing parameters for systematic application of the gradient and RF fields by the MRI pulse sequence and they control image contrast. The most basic sequences include free induction decay (FID), gradient recalled echo (GRE) and spin echo (SE) sequences. The pulse sequence and timing parameters are chosen to obtain tissue- or disease-specific contrast for diagnosis. Generally, shorter TE and TR values are associated with T_1 -

weighted imaging while longer TE and TR values are associated with T_2 -weighted imaging. T_2 -weighted imaging is more sensitive to pathologies compared to T_1 -weighted imaging because tissues associated with disease often have higher water content than normal, and thus have a longer T_2 and appear brighter (63). This is the case for GBM. However, other tissue contrasts can be obtained by adjusting TE and TR to exploit intrinsic differences in T_2 and T_1 . For example, rapid successive RF pulses (short TR), will prevent tissues with a long T_1 from recovering back to equilibrium, whereas tissue with shorter T_1 values still achieve appreciable relaxation. These parameter timings produce T_1 -weighted image contrast, preferentially highlighting tissues with faster spin-lattice relaxation or those enhanced by the presence of exogenous T_1 -contrast agents. T_1 -weighted imaging is useful for differentiation of white and gray matter in neuro-imaging (64).

The combination of the intrinsic physical properties of hydrogen nuclei and their large concentration in human tissue bound as water make it possible to non-invasively image their *in vivo* distribution with excellent tissue contrast, spatial resolution and SNR. In addition to exploiting intrinsic tissue properties with a range of MR imaging contrasts, healthy and diseased tissues can be further distinguished by the introduction of exogenous contrast agents. Paramagnetic contrast agents, such as Gd-DTPA have been used in the imaging of brain tumours to highlight morphological features undetectable with non-contrast enhanced imaging.

The use of paramagnetic contrast agents, which enhance the spin-lattice relaxation of neighbouring tissue, can increase the contrast between healthy tissue and tumour. However, there are several limitations associated with Gd-DTPA. Patients with impaired renal function cannot fully clear Gd-DTPA, which results in the accumulation of contrast

agent in tissue and could potentially lead to nephrogenic systemic fibrosis. Gd-DTPA does not readily penetrate the blood-brain-barrier (BBB) and, therefore, will only provide contrast enhancement of brain tissue if the BBB is disturbed. Lastly, Gd-DTPA lacks specificity as a contrast agent and does not directly target tumours. Gd-DTPA provides contrast enhancement in regions where the contrast agent can extravasate from the vasculature into the surrounding interstitial space in the event of an impaired BBB or blood-tumour barrier (BTB). Therefore, invasive therapies such as maximal surgical resection or anti-angiogenic treatment can falsely produce regions of tumour enhancement or lack of enhancement and ultimately may adversely affect the evaluation of treatment response. Given the limitations associated with anatomical imaging and detecting morphological changes in GBM, more sensitive and specific methods for tumour imaging are required to better diagnosis and treat this disease.

Diffusion and perfusion weighted MR imaging have been shown to be useful diagnostic tools when used in addition to standard anatomical imaging. Additional metrics obtained from DWI and PWI, such as tissue cellularity or blood perfusion, have been shown to be beneficial when discriminating responding and non-responding patients undergoing chemo- and radiotherapies (65). The ability to accurately assess tumour treatment response will prevent non-responding patients from undergoing weeks of ineffective therapy and will prevent responding patients from prematurely ending adjuvant therapy due to a misdiagnosis. Important data such as cerebral blood flow and volume can be measured with PWI, which is useful when determining blood delivery within the brain and specifically within or around the tumour. This is especially important when assessing the potential delivery of a chemotherapeutic to tumour tissue. In addition, PWI has been shown to be

very useful when differentiating between high or low grade glioma, lesion type or to aid in the identification of a primary or metastatic tumour (66).

The use of a panel of MRI imaging contrasts is known as multiparametric MRI (mpMRI). Depending upon the disease, a specific set of imaging contrasts are chosen, which are effective at discriminating a certain aspect of the pathology. For cancer, mpMRI provides complementary imaging information for the oncologist to assess treatment response or to understand tumour progression. The following section will outline the specific mpMRI techniques used in this preclinical research study.

1.6.1 T_1 -, T_2 -, Post-Gd T_1 -weighted and Diffusion MRI

The main mpMRI imaging contrasts used in this thesis include T_1 - and T_2 -weighted, post-Gd T_1 -weighted and DWI. As explained previously, spin-lattice (T_1) and spin-spin (T_2) relaxation are intrinsic tissue properties, which can be exploited to obtain contrast between tissues to improve the appearance of morphological features inside the brain or to differentiate between tumour and healthy tissue.

T_2 -weighted imaging emphasizes contrast based on water content within brain tissue. CSF and water have longer T_2 relaxation times relative to other brain tissue, therefore CSF and tissues with high water concentration will appear bright on a T_2 -weighted image.

This imaging technique is used in the clinical assessment of GBM because the inherent nature of tumour tissue creates hyperintense signals when compared to healthy tissue and aids in the identification and differentiation of tumour and healthy tissue. Due to the heterogenic cell composition of GBM and its irregular morphology, cells are coarsely

packed, and as a result, the larger fluid-filled extracellular space around tumour cells represents a larger volume fraction in tumours compared to healthy brain tissue (67). In addition, rapidly dividing tumour cells may cause fluid buildup or edema (68). The identification and differentiation of edema caused by GBM is important in the diagnosis and treatment of the disease because the edema may be misidentified as tumour mass and vice versa, amongst other factors. The presence of edema due to glioma may be unfavourable to the patient because of the increased peritumoural invasion and increased error in estimating tumour mass, which may have a large impact on the clinical planning of GBM (69).

T_1 -weighted imaging, sensitive to the longitudinal relaxation of tissue, is another useful endogenous imaging contrast. For example, CSF appears hypo-intense due to the long T_1 times associated with free water, while fat appears as hyper-intense due to the more efficient relaxation of protons in the large molecules associated with fatty lipids. T_1 -weighted imaging is less sensitive to pathologies than T_2 -weighted imaging due to the lack of tissue specific contrast enhancement related to disease. However, the use of paramagnetic contrast agents can alter tissue-specific contrast and post-Gd T_1 -weighted imaging can be used to identify and characterize brain lesions. Typically, pre-Gd T_1 -weighted imaging is done to establish a baseline. This image is compared to a second post-Gd T_1 -weighted image to determine which regions show increased signal corresponding to contrast agent delivery or accumulation. Since the BTB is much more permeable to Gd-DTPA than the BBB, perfused regions of tumours often show significant contrast enhancement post-injection (50). Contrast-enhanced imaging is especially useful when lesions are not detectable by T_2 -weighted imaging and may aid in differentiating edema

from tumour mass and regions of necrosis (70). T_1 -weighted imaging is the main imaging technique for assessing GBM response to treatment under the Macdonald criteria, but limitations exist associated with use of Gd-DTPA, which have been discussed previously (26, 27). Additional imaging techniques are often used as part of mpMRI to better identify tumour mass and to improve the detection of tumours and their response to treatment (29).

Diffusion-weighted imaging is an MRI technique that has previously shown to help the diagnosis and the evaluation of tumour treatment response (65). DWI measures the random translational (Brownian) motion of water molecules which is influenced by tissue structural integrity or cellularity (48, 71). The quantitative metric, known as the apparent diffusion coefficient (ADC), obtained from DWI has been shown to be inversely proportional to tissue cellularity (72, 73). Regional ADC measurement using DWI is a potential imaging biomarker for the assessment of treatment response (74), and the identification of necrosis.

The combined use of these different mpMRI techniques has provided a range of metrics to identify tumour lesions and tumour response to treatment. Each imaging technique can provide complementary information related to the tumour environment and, in combination, produce a more complete understanding of the biology of tumour progression.

1.7 Bioluminescence Imaging

Complementary imaging modalities are required to address the limitations of mpMRI, such as the inability to directly measure tumour cell viability and that anatomical changes are slow to occur and detect, and one possible modality that can directly measure relative

tumour cell viability is bioluminescence imaging (BLI)(75). BLI is a preclinical optical molecular imaging modality that benefits from high sensitivity (*e.g.*, single (76) to thousands of cells *in vivo* could be detected (77)), low cost, extremely high SNR due to the lack of intrinsic bioluminescence from tissue, the ability to image multiple animals within minutes, the ability to detect changes in tumour cell viability within a short time frame, and sufficient sensitivity to detect tumour cells immediately after implantation into an animal (77, 78). BLI has a wide range of applications in cancer imaging, such as, but not limited to, detection of metastatic formations throughout the mouse or rat body (76), evaluation of novel therapies in xenografted prostate cancer in mice (79) and ovarian cancer in mice (80), capacity to monitor the presence of genetically-modified bacteria and their role in inhibiting tumourigenesis in the orthotopic C6 rat model (81), and capacity to monitor effectiveness of gene therapy in a C6 glioma mouse model (59). However, BLI lacks the ability to obtain 3D anatomical imaging using various contrast mechanisms seen in mpMRI and is ultimately a preclinical imaging modality. Thus, the combined use of both BLI and mpMRI can address the limitations associated with each individual modality while benefiting from the advantages.

A requirement for BLI studies is that cell lines need to be genetically-engineered to express a luciferase reporter. There are many luciferase reporters available to use in BLI such as Firefly luciferase (FLuc) from *Photinus pyralis* (*i.e.*, the North American firefly), the red shifted *Luciola Italica* luciferase (Luc), or *Renilla* luciferase (RLuc) from *Renilla reniformis* (*i.e.*, the sea pansy). The most common reporter used is FLuc because it is the most efficient bioluminescence system to date and most studied. FLuc yields the highest light output efficiency *in vivo* and the standard FLuc emits green light which has minimal

light absorption from tissue. In addition, there is increased use of red-shifted luciferases such as *Luciola italica* (Italian firefly) for deep tissue imaging because of the decreased tissue light absorption (82). FLuc was first cloned in 1985 (78) and many years later, has found use in many preclinical *in vivo* studies (83-85). Several glioma cell lines have been genetically-engineered to express FLuc, for example Maguire *et al.* utilized a trimodal BLI approach to image the effect of soluble tumour necrosis factor-related apoptosis-inducing ligand on U87 cells implanted into the mouse brain (86). Sun *et al.* has used BLI to image and assess angiogenesis during progression of a orthotopic GL26 murine model (87). Jost *et al.* has utilized a BLI and MRI approach to image the progression of a Dihydrofolate reductase (DHFR) glioblastoma cell line in an orthotopic murine model (85). Lenten *et al.* has imaged the effect of suicide gene therapy in a orthotopic GL261 murine model (88).

For cells expressing Luc, bioluminescent light is produced by a catalytic reaction involving Luc and its substrate D-Luciferin (D-Luc), as well as the cofactors adenosine triphosphate (ATP), oxygen, and magnesium (Mg^{2+}). Figure 1-1 represents the catalytic Luc reaction which converts D-luciferin to oxyluciferin at the expenditure of ATP to adenosine monophosphate (AMP).

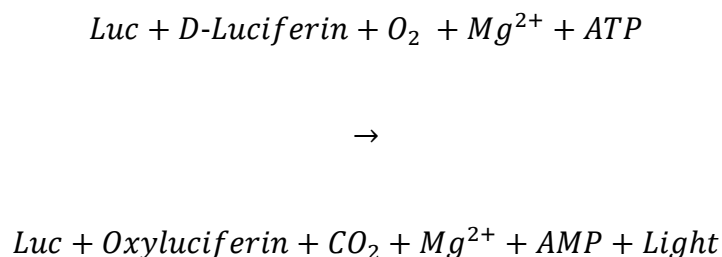


Figure 1-1. Bioluminescence chemical reaction equation.

In the presence of all the necessary cofactors (ATP, O₂ and Mg²⁺), the Luc enzyme can catalyze D-Luc into Oxyluciferin. This produces light in the 620-nm region, which can then be collected on a camera to produce BL images.

A benefit of BLI is the low background noise during the imaging because tissue does not naturally express luciferases nor do they naturally luminesce. Only viable tumour cells will produce light because only metabolically active tumour cells will be able to transcribe Luc, as well as produce the ATP needed to generate luminescence. Typical BLI equipment consists of a light-tight chamber and a cooled charge-coupled device (CCD) camera to reduce thermal noise. The chamber prevents external light from entering and its blackened interior surfaces prevents detection of scattered bioluminescent light from chamber walls. The cooled CCD camera sensitively collects light emitted from the bioluminescent source. The sensitivity of bioluminescence imaging largely relies on the depth of the luminescent cells, as optical imaging modalities have limited depth of penetration within tissue due to light scattering and tissue absorption. In addition, bioluminescence sensitivity is also influenced by the technology of the CCD camera itself, the amount of substrate, and level of luciferase activity per cell.

A typical BLI experiment begins with anesthetizing the rodent and injecting D-Luc in one of three substrate delivery methods; intraperitoneal, intravenous, or subcutaneous. Intraperitoneal injections are the most common route of substrate delivery due to the extended and high bioluminescence output profile, as imaging is typically done when light output has peaked to reduce variability between animals. However, any variations in D-Luc absorption can have an influence on bioluminescent signal, such as the injection of substrate into the gut rather than the intraperitoneal space. Intravenous injections require lower doses to achieve similar bioluminescence intensities but are quick to peak and clear through the body. Subcutaneous injections can be used to avoid the shortcomings associated with intraperitoneal injections but have a much longer lag time associated with time to signal peak (89).

By combining two imaging modalities, mpMRI and BLI, that provide complementary information, the limitations associated with each modality can be minimized while obtaining a large range of useful, imaging metrics. BLI provides high SNR images, sensitive cell specific information, a reliable measure of the relative number of viable tumour cells over time and immediately after tumour implantation into an animal while minimizing cost and time with the ability to image multiple animals within a short time frame. However, BLI is limited to 2D preclinical imaging due to a lack of penetration depth within tissue associated with light scattering and tissue absorption, which can reduce sensitivity and limit spatial information within deeper layers of animal tissue. BLI is dependent on substrate delivery for signal production, thus has similar limitations associated with imaging modalities that rely on substrate delivery (*e.g.*, PET/SPECT), particularly lack of enhancement in ill-perfused regions. Whereas mpMRI is the gold

standard for the diagnosis and assessment of GBM and its response to treatment with various contrast mechanisms. However, mpMRI lacks the sensitivity and ability to directly measure tumour cell viability.

1.8 Thesis Overview

Conventional MRI (FLAIR/ T_2 /post-Gd T_1) is a powerful imaging modality for the diagnosis and assessment of tumour response to therapy. However, this imaging modality is generally restricted to only providing anatomical information, which may be inaccurate and changes may be slow to occur, ultimately affecting the planning and success of therapy. Multiparametric MRI consists of a larger suite of imaging techniques, which include DWI and PWI, capable of providing functional information alongside anatomy. These imaging techniques have been shown to improve the diagnosis of GBM and assessment of its response to therapy (90). Utilizing additional imaging metrics can provide information which can aid to differentiate radiation necrosis from recurrent GBM, which is usually indistinguishable in conventional post-Gd T_1 -weighted MRI. The ability to obtain more than one piece of information of GBM will provide the clinician with a better understanding of tumour behavior and can improve assessment and treatment of GBM. Although mpMRI addresses and improves on the limitations of conventional MRI, there are no imaging methods or techniques in mpMRI that can measure tumour cell viability. A complementary imaging modality known as BLI may be best suited to address this limitation of mpMRI in preclinical animal models of GBM as it provides a direct measurement of relative tumour cell viability with high sensitivity and specificity.

The purpose of my thesis was to develop a multimodality imaging framework using both BLI and mpMRI to characterize the natural progression of orthotopic C6 glioblastoma multiforme expressing red-shifted *Luciola Italica* luciferase (C6Luc) cells in Wistar rats. The naïve C6 cells were genetically modified using lentiviral vectors to introduce the GFP-Luc gene into the genome of cells. These cells and the C6 cell line, when orthotopically implanted into the brain of Wistar rats, closely mimics the diffuse growth development of human GBM and shares several histopathological and genetic markers. The motivation behind this thesis was to characterize longitudinal C6Luc tumour growth using both BLI and mpMRI. Although previous studies have reported the use of BLI in monitoring GBM development (85) and response to therapy (91), no study, to date, has applied both BLI and mpMRI to characterize the natural progression of C6Luc in an orthotopic rat model. This thesis aims to characterize the natural progression of orthotopic GBM in a rat model using both BLI and mpMRI. Current literature does not provide information on how these two metrics, cellular viability and volumetric tumour metrics, are related and how they describe the progression of GBM in a rat. I hypothesized that measurements of tumour cellular viability are required to better understand tumour biology and behavior, and that tumour cell viability would increase proportionally with measures of tumour volume determined with mpMRI.

In chapter 2, the multimodality imaging framework of BLI and mpMRI was applied to longitudinally imaging orthotopic C6Luc tumours in Wistar rats. Despite the initial hypothesis, the results suggested that the opposite was true. BLI measurements of tumour cell viability did not increase proportional to tumour burden determined by mpMRI. Chapter 2 will offer an in-depth discussion and analysis of the possible factors contributing

to this discordance between two separate measurements of tumour burden and I present three potential hypotheses to explain the disproportionate changes in BLI and mpMRI measurements of tumour burden. We also present 2 lines of evidence supporting the hypothesis that the discordance between BLI and mpMRI measures are due in part to an increase in necrosis (*i.e.*, decreased tumour cell viability). First, fully co-registered ADC maps to post-Gd T_1 -weighted MR images provide evidence that there is a decrease in tissue cellularity within regions of non-contrast enhancement (*i.e.*, less perfused). In addition, fully co-registered whole brain histology offers qualitative evidence that necrosis is the likely cause of proportional changes in BLI and mpMRI measurements.

Chapter 3 summarizes, concludes, and highlights the findings in chapter 2, which provided evidence to the usefulness of combining both BLI and mpMRI to characterize the progression of orthotopic C6 GBM tumours. The use of BLI provides a direct measure of relative tumour cell viability, a metric unobtainable in mpMRI, but lacks the anatomical and functional information obtainable with mpMRI. The complementary nature of these two imaging modalities will provide a better understanding of GBM progression in an orthotopic C6 rat model. Future directions for this research and suggestions for improvement of our methods are also provided in this chapter.

1.9 References

1. Canadian Cancer Society. Canadian Cancer Society's Advisory Committee on Cancer Statistics. Canadian Cancer Statistics 2017. 2017.
2. Ostrom QT, Gittleman H, de Blank PM, Finlay JL, Gurney JG, McKean-Cowdin R, et al. American Brain Tumor Association Adolescent and Young Adult Primary Brain and Central Nervous System Tumors Diagnosed in the United States in 2008-2012. *Neuro Oncol.* 2016;18 Suppl 1:i1-i50.

3. Gladson CL, Prayson RA, Liu WM. The pathobiology of glioma tumors. *Annu Rev Pathol.* 2010;5:33-50.
4. Louis DN, Ohgaki H, Wiestler OD, Cavenee WK, Burger PC, Jouvet A, et al. The 2007 WHO classification of tumours of the central nervous system. *Acta Neuropathol.* 2007;114(2):97-109.
5. Urbanska K, Sokolowska J, Szmidt M, Sysa P. Glioblastoma multiforme - an overview. *Contemp Oncol (Pozn).* 2014;18(5):307-12.
6. Zong H, Verhaak RG, Canoll P. The cellular origin for malignant glioma and prospects for clinical advancements. *Expert Rev Mol Diagn.* 2012;12(4):383-94.
7. Simpson JR, Horton J, Scott C, Curran WJ, Rubin P, Fischbach J, et al. Influence of location and extent of surgical resection on survival of patients with glioblastoma multiforme: results of three consecutive Radiation Therapy Oncology Group (RTOG) clinical trials. *Int J Radiat Oncol Biol Phys.* 1993;26(2):239-44.
8. Chicoine MR, Silbergeld DL. Invading C6 glioma cells maintaining tumorigenicity. *J Neurosurg.* 1995;83(4):665-71.
9. Karcher S, Steiner HH, Ahmadi R, Zoubaa S, Vasvari G, Bauer H, et al. Different angiogenic phenotypes in primary and secondary glioblastomas. *Int J Cancer.* 2006;118(9):2182-9.
10. Chang JE, Khuntia D, Robins HI, Mehta MP. Radiotherapy and radiosensitizers in the treatment of glioblastoma multiforme. *Clin Adv Hematol Oncol.* 2007;5(11):894-902, 7-15.
11. Gerstner ER, Batchelor TT. Antiangiogenic therapy for glioblastoma. *Cancer J.* 2012;18(1):45-50.
12. Cho DY, Yang WK, Lee HC, Hsu DM, Lin HL, Lin SZ, et al. Adjuvant immunotherapy with whole-cell lysate dendritic cells vaccine for glioblastoma multiforme: a phase II clinical trial. *World Neurosurg.* 2012;77(5-6):736-44.
13. Altioek N, Ersoz M, Koyuturk M. Estradiol induces JNK-dependent apoptosis in glioblastoma cells. *Oncol Lett.* 2011;2(6):1281-5.
14. von Neubeck C, Seidlitz A, Kitzler HH, Beuthien-Baumann B, Krause M. Glioblastoma multiforme: emerging treatments and stratification markers beyond new drugs. *Br J Radiol.* 2015;88(1053):20150354.
15. Mehta AI, Kanaly CW, Friedman AH, Bigner DD, Sampson JH. Monitoring radiographic brain tumor progression. *Toxins (Basel).* 2011;3(3):191-200.
16. Mabray MC, Barajas RF, Jr., Cha S. Modern brain tumor imaging. *Brain Tumor Res Treat.* 2015;3(1):8-23.

17. Horska A, Barker PB. Imaging of brain tumors: MR spectroscopy and metabolic imaging. *Neuroimaging Clin N Am*. 2010;20(3):293-310.
18. Lee MH, Smyser CD, Shimony JS. Resting-state fMRI: a review of methods and clinical applications. *AJNR Am J Neuroradiol*. 2013;34(10):1866-72.
19. Schmainda KM. Diffusion-weighted MRI as a biomarker for treatment response in glioma. *CNS Oncol*. 2012;1(2):169-80.
20. Fink JR, Muzi M, Peck M, Krohn KA. Multimodality Brain Tumor Imaging: MR Imaging, PET, and PET/MR Imaging. *J Nucl Med*. 2015;56(10):1554-61.
21. Puttick S, Bell C, Dowson N, Rose S, Fay M. PET, MRI, and simultaneous PET/MRI in the development of diagnostic and therapeutic strategies for glioma. *Drug Discov Today*. 2015;20(3):306-17.
22. Carvalho PA, Schwartz RB, Alexander E, 3rd, Garada BM, Zimmerman RE, Loeffler JS, et al. Detection of recurrent gliomas with quantitative thallium-201/technetium-99m HMPAO single-photon emission computerized tomography. *J Neurosurg*. 1992;77(4):565-70.
23. Kim EE, Chung SK, Haynie TP, Kim CG, Cho BJ, Podoloff DA, et al. Differentiation of residual or recurrent tumors from post-treatment changes with F-18 FDG PET. *Radiographics*. 1992;12(2):269-79.
24. Schultz S, Pinsky GS, Wu NC, Chamberlain MC, Rodrigo AS, Martin SE. Fine needle aspiration diagnosis of extracranial glioblastoma multiforme: Case report and review of the literature. *Cytojournal*. 2005;2:19.
25. Young RM, Jamshidi A, Davis G, Sherman JH. Current trends in the surgical management and treatment of adult glioblastoma. *Ann Transl Med*. 2015;3(9):121.
26. Macdonald DR, Cascino TL, Schold SC, Jr., Cairncross JG. Response criteria for phase II studies of supratentorial malignant glioma. *J Clin Oncol*. 1990;8(7):1277-80.
27. Quant EC, Wen PY. Response assessment in neuro-oncology. *Curr Oncol Rep*. 2011;13(1):50-6.
28. Wen PY, Macdonald DR, Reardon DA, Cloughesy TF, Sorensen AG, Galanis E, et al. Updated response assessment criteria for high-grade gliomas: response assessment in neuro-oncology working group. *J Clin Oncol*. 2010;28(11):1963-72.
29. Meier R, Braren R, Kosanke Y, Bussemer J, Neff F, Wildgruber M, et al. Multimodality multiparametric imaging of early tumor response to a novel antiangiogenic therapy based on anticalins. *PLoS One*. 2014;9(5):e94972.
30. Lenting K, Verhaak R, Ter Laan M, Wesseling P, Leenders W. Glioma: experimental models and reality. *Acta Neuropathol*. 2017;133(2):263-82.

31. Jacobs VL, Valdes PA, Hickey WF, De Leo JA. Current review of in vivo GBM rodent models: emphasis on the CNS-1 tumour model. *ASN Neuro*. 2011;3(3):e00063.
32. Candolfi M, Curtin JF, Nichols WS, Muhammad AG, King GD, Pluhar GE, et al. Intracranial glioblastoma models in preclinical neuro-oncology: neuropathological characterization and tumor progression. *J Neurooncol*. 2007;85(2):133-48.
33. Palmowski K, Winz O, Rix A, Bzyl J, Behrendt FF, Verburg FA, et al. Accuracy of a clinical PET/CT vs. a preclinical muPET system for monitoring treatment effects in tumour xenografts. *Eur J Radiol*. 2013;82(8):1318-24.
34. Barth RF, Kaur B. Rat brain tumor models in experimental neuro-oncology: the C6, 9L, T9, RG2, F98, BT4C, RT-2 and CNS-1 gliomas. *J Neurooncol*. 2009;94(3):299-312.
35. Benda P, Lightbody J, Sato G, Levine L, Sweet W. Differentiated rat glial cell strain in tissue culture. *Science*. 1968;161(3839):370-1.
36. Schmidek HH, Nielsen SL, Schiller AL, Messer J. Morphological studies of rat brain tumors induced by N-nitrosomethylurea. *J Neurosurg*. 1971;34(3):335-40.
37. Auer RN, Del Maestro RF, Anderson R. A simple and reproducible experimental in vivo glioma model. *Can J Neurol Sci*. 1981;8(4):325-31.
38. Sibenaller ZA, Etame AB, Ali MM, Barua M, Braun TA, Casavant TL, et al. Genetic characterization of commonly used glioma cell lines in the rat animal model system. *Neurosurg Focus*. 2005;19(4):E1.
39. Schlegel J, Piontek G, Kersting M, Schuermann M, Kappler R, Scherthan H, et al. The p16/Cdkn2a/Ink4a gene is frequently deleted in nitrosourea-induced rat glial tumors. *Pathobiology*. 1999;67(4):202-6.
40. Grobbs B, De Deyn PP, Slegers H. Rat C6 glioma as experimental model system for the study of glioblastoma growth and invasion. *Cell Tissue Res*. 2002;310(3):257-70.
41. Asai A, Miyagi Y, Sugiyama A, Gamanuma M, Hong SH, Takamoto S, et al. Negative effects of wild-type p53 and s-Myc on cellular growth and tumorigenicity of glioma cells. Implication of the tumor suppressor genes for gene therapy. *J Neurooncol*. 1994;19(3):259-68.
42. Liao J, Xia R, Liu T, Feng H, Ai H, Song B, et al. In vivo dynamic monitoring of the biological behavior of labeled C6 glioma by MRI. *Mol Med Rep*. 2013;7(5):1397-402.
43. Batchelor TT, Reardon DA, de Groot JF, Wick W, Weller M. Antiangiogenic therapy for glioblastoma: current status and future prospects. *Clin Cancer Res*. 2014;20(22):5612-9.

44. Gridley DS, Timiryasova TM, Miller GM, Andres ML, Dutta-Roy R, Bayeta EJ, et al. Evaluation of TNF-alpha/Bax gene therapy and radiation against C6 glioma xenografts. *Technol Cancer Res Treat*. 2003;2(1):41-50.
45. Zhao S, Zhang X, Zhang J, Zhang J, Zou H, Liu Y, et al. Intravenous administration of arsenic trioxide encapsulated in liposomes inhibits the growth of C6 gliomas in rat brains. *J Chemother*. 2008;20(2):253-62.
46. Kao HW, Chiang SW, Chung HW, Tsai FY, Chen CY. Advanced MR imaging of gliomas: an update. *Biomed Res Int*. 2013;2013:970586.
47. Liu J, Zhou J, Li J, Zhang J, Zhang P, Liu B. Evaluation of rat C6 malignant glioma using spectral computed tomography. *Experimental and Therapeutic Medicine*. 2017;14(2):1037-44.
48. Holodny AI, Ollenschlager M. Diffusion imaging in brain tumors. *Neuroimaging Clin N Am*. 2002;12(1):107-24, x.
49. Asanuma T, Doblaz S, Tesiram YA, Saunders D, Cranford R, Pearson J, et al. Diffusion tensor imaging and fiber tractography of C6 rat glioma. *J Magn Reson Imaging*. 2008;28(3):566-73.
50. Huhndorf M, Moussavi A, Kramann N, Will O, Hattermann K, Stadelmann C, et al. Alterations of the Blood-Brain Barrier and Regional Perfusion in Tumor Development: MRI Insights from a Rat C6 Glioma Model. *PLoS One*. 2016;11(12):e0168174.
51. Yu TG, Feng Y, Feng XY, Dai JZ, Qian HJ, Huang Z. Prognostic factor from MR spectroscopy in rat with astrocytic tumour during radiation therapy. *Br J Radiol*. 2015;88(1045):20140418.
52. Day SE, Kettunen MI, Cherukuri MK, Mitchell JB, Lizak MJ, Morris HD, et al. Detecting response of rat C6 glioma tumors to radiotherapy using hyperpolarized [1-13C]pyruvate and 13C magnetic resonance spectroscopic imaging. *Magn Reson Med*. 2011;65(2):557-63.
53. Assadian S, Aliaga A, Del Maestro RF, Evans AC, Bedell BJ. FDG-PET imaging for the evaluation of antiglioma agents in a rat model. *Neuro Oncol*. 2008;10(3):292-9.
54. Wyss MT, Spaeth N, Biollaz G, Pahnke J, Alessi P, Trachsel E, et al. Uptake of 18F-Fluorocholine, 18F-FET, and 18F-FDG in C6 gliomas and correlation with 131I-SIP(L19), a marker of angiogenesis. *J Nucl Med*. 2007;48(4):608-14.
55. Wang H, Zhang Y, Yu W, Zhao X, Xue Y, Xu H. Radiosensitizing effect of irisquinone on glioma through the downregulation of HIF-1alpha evaluated by 18F-FDG and 18F-FMISO PET/CT. *Nucl Med Commun*. 2016;37(7):705-14.

56. Yeung TP, Kurdi M, Wang Y, Al-Khazraji B, Morrison L, Hoffman L, et al. CT perfusion imaging as an early biomarker of differential response to stereotactic radiosurgery in C6 rat gliomas. *PLoS One*. 2014;9(10):e109781.
57. Riemann B, Konemann S, Popping D, Kopka K, Weckesser M, Willich N, et al. Early effects of irradiation on [(123)I]-IMT and [(18)F]-FDG uptake in rat C6 glioma cells. *Strahlenther Onkol*. 2004;180(7):434-41.
58. Yeom CJ, Chung JK, Kang JH, Jeon YH, Kim KI, Jin YN, et al. Visualization of hypoxia-inducible factor-1 transcriptional activation in C6 glioma using luciferase and sodium iodide symporter genes. *J Nucl Med*. 2008;49(9):1489-97.
59. Jang SJ, Kang JH, Kim KI, Lee TS, Lee YJ, Lee KC, et al. Application of bioluminescence imaging to therapeutic intervention of herpes simplex virus type I - Thymidine kinase/ganciclovir in glioma. *Cancer Lett*. 2010;297(1):84-90.
60. Xi G, Mania-Farnell B, Rajaram V, Mayanil CS, Soares MB, Tomita T, et al. Efficacy of interstitial continuous vincristine infusion in a bioluminescent rodent intracranial tumor model. *J Neurooncol*. 2012;106(2):261-70.
61. Xi G, Rajaram V, Mania-Farnell B, Mayanil CS, Soares MB, Tomita T, et al. Efficacy of vincristine administered via convection-enhanced delivery in a rodent brainstem tumor model documented by bioluminescence imaging. *Childs Nerv Syst*. 2012;28(4):565-74.
62. Bojorquez JZ, Bricq S, Acquitter C, Brunotte F, Walker PM, Lalande A. What are normal relaxation times of tissues at 3 T? *Magn Reson Imaging*. 2017;35:69-80.
63. Bitar R, Leung G, Perng R, Tadros S, Moody AR, Sarrazin J, et al. MR pulse sequences: what every radiologist wants to know but is afraid to ask. *Radiographics*. 2006;26(2):513-37.
64. Kalpathy-Cramer J, Gerstner ER, Emblem KE, Andronesi O, Rosen B. Advanced magnetic resonance imaging of the physical processes in human glioblastoma. *Cancer Res*. 2014;74(17):4622-37.
65. Galban CJ, Lemasson B, Hoff BA, Johnson TD, Sundgren PC, Tsien C, et al. Development of a Multiparametric Voxel-Based Magnetic Resonance Imaging Biomarker for Early Cancer Therapeutic Response Assessment. *Tomography*. 2015;1(1):44-52.
66. Essig M, Nguyen TB, Shiroishi MS, Saake M, Provenzale JM, Enterline DS, et al. Perfusion MRI: the five most frequently asked clinical questions. *AJR Am J Roentgenol*. 2013;201(3):W495-510.
67. Young RJ, Knopp EA. Brain MRI: tumor evaluation. *J Magn Reson Imaging*. 2006;24(4):709-24.

68. Papadopoulos MC, Saadoun S, Binder DK, Manley GT, Krishna S, Verkman AS. Molecular mechanisms of brain tumor edema. *Neuroscience*. 2004;129(4):1011-20.
69. Lin ZX. Glioma-related edema: new insight into molecular mechanisms and their clinical implications. *Chin J Cancer*. 2013;32(1):49-52.
70. Donahue MJ, Blakeley JO, Zhou J, Pomper MG, Laterra J, van Zijl PC. Evaluation of human brain tumor heterogeneity using multiple T1-based MRI signal weighting approaches. *Magn Reson Med*. 2008;59(2):336-44.
71. Hygino da Cruz LC, Jr., Vieira IG, Domingues RC. Diffusion MR imaging: an important tool in the assessment of brain tumors. *Neuroimaging Clin N Am*. 2011;21(1):27-49, vii.
72. Fan G, Zang P, Jing F, Wu Z, Guo Q. Usefulness of diffusion/perfusion-weighted MRI in rat gliomas: correlation with histopathology. *Acad Radiol*. 2005;12(5):640-51.
73. Poptani H, Puumalainen AM, Grohn OH, Loimas S, Kainulainen R, Yla-Herttuala S, et al. Monitoring thymidine kinase and ganciclovir-induced changes in rat malignant glioma in vivo by nuclear magnetic resonance imaging. *Cancer Gene Ther*. 1998;5(2):101-9.
74. Padhani AR, Liu G, Koh DM, Chenevert TL, Thoeny HC, Takahara T, et al. Diffusion-weighted magnetic resonance imaging as a cancer biomarker: consensus and recommendations. *Neoplasia*. 2009;11(2):102-25.
75. Koo V, Hamilton PW, Williamson K. Non-invasive in vivo imaging in small animal research. *Cell Oncol*. 2006;28(4):127-39.
76. Kim JB, Urban K, Cochran E, Lee S, Ang A, Rice B, et al. Non-invasive detection of a small number of bioluminescent cancer cells in vivo. *PLoS One*. 2010;5(2):e9364.
77. Zinn KR, Chaudhuri TR, Szafran AA, O'Quinn D, Weaver C, Dugger K, et al. Noninvasive bioluminescence imaging in small animals. *ILAR J*. 2008;49(1):103-15.
78. Sadikot RT, Blackwell TS. Bioluminescence imaging. *Proc Am Thorac Soc*. 2005;2(6):537-40, 11-2.
79. Brakenhielm E, Burton JB, Johnson M, Chavarria N, Morizono K, Chen I, et al. Modulating metastasis by a lymphangiogenic switch in prostate cancer. *Int J Cancer*. 2007;121(10):2153-61.
80. Kanerva A, Zinn KR, Chaudhuri TR, Lam JT, Suzuki K, Uil TG, et al. Enhanced therapeutic efficacy for ovarian cancer with a serotype 3 receptor-targeted oncolytic adenovirus. *Mol Ther*. 2003;8(3):449-58.

81. Chen JQ, Zhan YF, Wang W, Jiang SN, Li XY. The engineered *Salmonella typhimurium* inhibits tumorigenesis in advanced glioma. *Onco Targets Ther.* 2015;8:2555-63.
82. Badr CE, Tannous BA. Bioluminescence imaging: progress and applications. *Trends Biotechnol.* 2011;29(12):624-33.
83. Edinger M, Cao YA, Hornig YS, Jenkins DE, Verneris MR, Bachmann MH, et al. Advancing animal models of neoplasia through in vivo bioluminescence imaging. *Eur J Cancer.* 2002;38(16):2128-36.
84. Soling A, Rainov NG. Bioluminescence imaging in vivo - application to cancer research. *Expert Opin Biol Ther.* 2003;3(7):1163-72.
85. Jost SC, Collins L, Travers S, Piwnica-Worms D, Garbow JR. Measuring brain tumor growth: combined bioluminescence imaging-magnetic resonance imaging strategy. *Mol Imaging.* 2009;8(5):245-53.
86. Maguire CA, Bovenberg MS, Crommentuijn MH, Niers JM, Kerami M, Teng J, et al. Triple bioluminescence imaging for in vivo monitoring of cellular processes. *Mol Ther Nucleic Acids.* 2013;2:e99.
87. Sun A, Hou L, Prugpichailers T, Dunkel J, Kalani MA, Chen X, et al. Firefly luciferase-based dynamic bioluminescence imaging: a noninvasive technique to assess tumor angiogenesis. *Neurosurgery.* 2010;66(4):751-7; discussion 7.
88. Leten C, Trekker J, Struys T, Dresselaers T, Gijssbers R, Vande Velde G, et al. Assessment of bystander killing-mediated therapy of malignant brain tumors using a multimodal imaging approach. *Stem Cell Res Ther.* 2015;6:163.
89. Close DM, Xu T, Saylor GS, Ripp S. In vivo bioluminescent imaging (BLI): noninvasive visualization and interrogation of biological processes in living animals. *Sensors (Basel).* 2011;11(1):180-206.
90. Yoon RG, Kim HS, Koh MJ, Shim WH, Jung SC, Kim SJ, et al. Differentiation of Recurrent Glioblastoma from Delayed Radiation Necrosis by Using Voxel-based Multiparametric Analysis of MR Imaging Data. *Radiology.* 2017:161588.
91. Luwor RB, Stylli SS, Kaye AH. Using bioluminescence imaging in glioma research. *J Clin Neurosci.* 2015;22(5):779-84.

Chapter 2

2 Multiparametric Magnetic Resonance Imaging and Bioluminescence Imaging Characterization of an Orthotopic Rat Model of Glioblastoma

2.1 Introduction

Glioma is the most common malignant form of primary brain tumour with the highest mortality rate (1). Grade IV glioblastoma multiforme (GBM) is the most aggressive, invasive and lethal form of glioma and accounts for approximately 50% of all glioma cases (2-4). GBM is considered incurable and patient survival after diagnosis is approximately 15-18 months despite aggressive treatment paradigms such as combined surgical resection (5), radiotherapy, and temozolomide chemotherapy (6, 7). These highly-aggressive malignancies have a tendency to undergo necrosis (8), are highly invasive and proliferative (9, 10), have robust angiogenesis, and are resistant to apoptosis (11, 12). The combination of these factors contribute to therapeutic resistance and nearly 100% recurrence rates. To improve our understanding of the progression of this devastating disease and for enhanced evaluation of new treatment regimens, novel complementary methods for non-invasive assessment of GBM tumours in both preclinical GBM models and GBM patients are needed.

Preclinical mouse and rat models of glioma have been invaluable for understanding GBM progression, evaluating novel therapeutic strategies, and for developing new imaging techniques for better tumour characterization (13-15). In particular, the orthotopic C6 rat

model has provided a great deal of insight into biological mechanisms and progression of GBM (9, 14, 16-18). The C6 cell line was first developed by the Sweet laboratory in the 1960s by repeated intravenous administration of the carcinogenic alkylating agent, N-methyl-N-nitrosourea to outbred adult Wistar rats (19, 20). C6 tumours share several specific tumour markers found in human GBM such as increased Ras pathway activity, increased platelet-derived growth factor-beta, insulin-like growth factor 1, epidermal growth factor receptor, human epidermal growth factor receptor 3 and glial fibrillary acidic protein expression (14). C6 tumours also share histopathological features found in human GBM such as a diffuse infiltrative pattern (9). Due to these favourable characteristics, C6 tumour-bearing rats have been used to evaluate therapeutic efficacy of various treatment regimens such as chemotherapy (16), radiotherapy (17), and cytotoxic gene therapy (18).

To facilitate improved evaluation of treatments and a better understanding of tumours in the C6 model, numerous groups have utilized clinically-relevant imaging tools such as positron emission tomography (PET)(21), computed tomography (CT)(22), and magnetic resonance imaging (MRI)(23). MRI has become the standard of care for the detection, staging, and assessment of treatment response in glioma patients (24). Benefits of MRI are the ability to collect high resolution images with excellent soft tissue contrast without the use of ionizing radiation, allowing changes in tumour morphology and function to be monitored over time. Various MR contrast mechanisms are available, which can accentuate different tumour features allowing better identification of tumour mass from other confounding features such as edema or hemorrhage. Multiparametric MRI (mpMRI) involves collection of a suite of MRI images with different contrast mechanisms, providing both functional and anatomical information about tumours such as total tumour volume,

contrast-enhanced tumour volume, ADC, and tumour perfusion (25). Multiparametric MRI has previously been applied to the orthotopic C6 rat model (23, 26-28). For instance, Liao *et al.*, working with the C6 rat model used MRI to gather information about tumour volume and location, blood brain barrier integrity, and edema (29). However, MRI lacks a sensitive biomarker to measure tumour cellular viability and any changes in tumour size are slow to detect in MRI because morphological changes are slow to occur.

In addition to clinical imaging tools, preclinical imaging tools can provide additional valuable information on tumour biology. Bioluminescence imaging (BLI) is a molecular imaging modality that is dependent on engineering cells to express a luciferase reporter gene (*e.g.*, red-shifted *Luciola Italica* luciferase (Luc)) prior to implantation into animals. Thereafter, one can image the light produced by these engineered cells with a cooled charge-coupled device camera following systemic administration of the appropriate luciferin substrate (*e.g.*, D-luciferin)(30). The main advantage of BLI is the ability to sensitively track the relative viability of cells over time due to the requirement of cells to transcribe the reporter, as well as the use of ATP as a co-factor for light production. As observed in other cancer models (31, 32), changes in BLI measures of cellular viability may or may not change proportionally to MRI measures of total tumour burden, meaning BLI provides complementary information to MRI for tracking tumour progression. BLI has been previously applied to the C6 model. Xi *et al.* used BLI to track treatment response of vincristine administration in Fischer 344 rats carrying luciferase-expressing C6 tumours in the brainstem (33). Hwang *et al.* applied BLI to monitor tumour growth in mice bearing luciferase-expressing C6 cells in the hind limb (34). Thus, both mpMRI and BLI have separately been applied to the C6 model (33, 35), and this imaging study was the first to

compare longitudinal BLI and mpMRI data in untreated orthotopic C6 rat glioma with histology at end-point. Current literature provides little information to how BLI and mpMRI metrics of tumour burden relate in the C6 GBM rat model. Although these two metrics may be understood separately, it is important to characterize the two metrics in one study to fully understand the nature of tumour progression. We hope to be able to show the usefulness of BLI as a measurement of tumour viability, but to also show that a multimodality imaging framework is required to fully understand tumour biology. The goal of this chapter was to apply a multimodality imaging framework to the orthotopic C6Luc rat model to characterize the natural progression of GBM with both BLI and mpMRI. We hypothesized that metrics of tumour viability in BLI would not only increase proportionally with metrics of tumour volume in mpMRI, but would also provide complementary information required to better understand the tumour biology during progression. We found that the combination of these imaging methods provided new insights into GBM development in this model, and will be useful for more precise future preclinical evaluation of the effectiveness of new treatment strategies to help combat this disease compared to utilizing a single imaging modality.

2.2 Methods and Materials

2.2.1 Cells

C6 rat glioma cells (CCL-107, American Type Culture Collection, Manassas, VA) were grown in Ham's F-12K (Kaighn's) medium (Invitrogen, Carlsbad, CA, USA) containing 2.5% fetal bovine serum (FBS), 15% horse serum and 1% penicillin-streptomycin. All cells were grown at 37°C in a 5% CO₂ incubator. Cells were regularly confirmed to be

mycoplasma-negative using the MycoAlert Mycoplasma Detection Kit (Lonza, Basel, Switzerland).

2.2.2 Lentiviral Transduction

Self-inactivating lentiviral particles co-expressing red-shifted *Luciola Italica* luciferase (Luc) and green fluorescence protein (GFP) under the control of the Ubiquitin C promoter were used (RediFect; PerkinElmer, Waltham, Massachusetts, USA). For efficient co-expression Luc and GFP are separated by a T2A “self-cleaving” linker peptide in this vector. C6 glioma cells were transduced for 24 hours at a viral multiplicity of infection (MOI) of 50 using polybrene (8 µg/mL). Following transduction, engineered C6 cells that had the highest co-expression of GFP and Luc (C6Luc) were isolated by fluorescence-activated cell sorting (FACS) using a BD FACSAria™ III sorter (BD Biosciences, Franklin Lakes, New Jersey, USA). During the first sort, cells were gated to obtain the brightest GFP expressing cells (4.52% of all cells) and the cells were propagated and expanded

(Figure 2-1C). During the second sort, cells with the top 10% fluorescence intensity were selected for and expanded, as shown in Figures 2-1C & D.

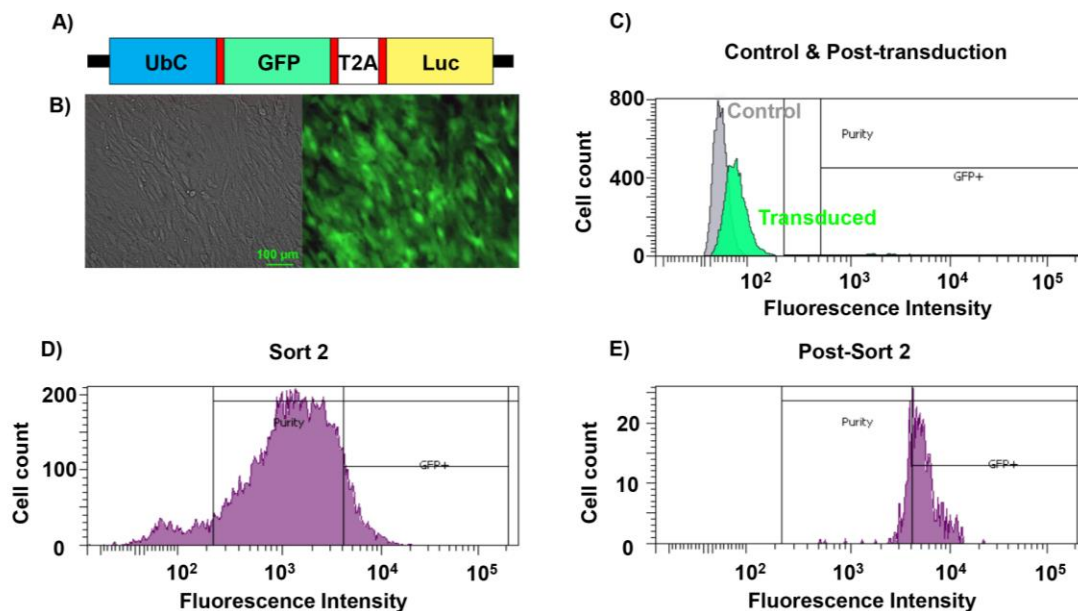


Figure 2-1. Lentiviral Engineering of C6 Glioma Cells with Reporter Genes.

A) Expression cassette of Luc-GFP lentiviral vectors. UbC = Ubiquitin C promoter; GFP = green fluorescent protein; Luc = red-shifted *Luciola Italica* luciferase; T2A = self-cleaving linker peptide. **B)** left: bright field image of C6Luc cells post-sort *in vitro*, right: fluorescence image of GFP expression *in vitro*. Scale bar = 100 μm . **C)** FACS of control (naïve C6; gray) and C6Luc (green) cells post-transduction. Cells were gated to obtain the brightest GFP expressing cells; 4.52% of all glioma cells. **D)** Second FACS to select the top 10% of GFP expressing cells after propagation of highest GFP expressing cells from the initial FACS. **E)** Immediately after the second FACS (D), a FACS analysis was performed to evaluate GFP expression in the final population (100% of cells expressed GFP).

2.2.3 *In Vitro* Cell Analysis

2.2.3.1 Doubling Rate

C6 and C6Luc cells were seeded into individual wells of a six-well plate (2×10^3 cells/well; $n = 3$ per cell type). An additional three six-well plates were seeded with C6Luc cells incubated with $150 \mu\text{g/mL}$ of D-luciferin (C6Luc150). The total cell number in each well was determined using a haemocytometer, every 24 hours up to 144 hours. The doubling rates of the cell lines were determined using the model, $y = a \times 2^{t/b}$. Here y is the cell count, a is the number of cells in the initial seed, t is the amount of time elapsed in hours, and b is the doubling time of the cells in hours. A MATLAB script employing the non-linear least squares Trust-Region algorithm from the Curve Fitting Toolbox (MATLAB 2016b, The MathWorks Inc., Natick, MA, USA 2000) was used to determine parameters a and b .

2.2.3.2 Radiance vs Cell Number

Known numbers of C6Luc cells (1×10^6 , 5×10^5 , 2.5×10^5 , 1.25×10^5 , 6.25×10^4 and 3.13×10^4) were seeded into individual wells and incubated for 24 hours. D-luciferin ($150 \mu\text{g/mL}$) was added to each well, and plates were imaged five minutes later with an IVIS Lumina XRMS In Vivo Imaging System (PerkinElmer, MA, USA). Images were analyzed using Living Image Software (IVIS Imaging Systems, PerkinElmer, MA, USA) to obtain the average radiance (photons/sec/cm²/steradian) per well.

2.2.4 Orthotopic C6 Glioma Rat Model

All animal procedures were performed in accordance with relevant guidelines and regulations stipulated by an animal use protocol approved by the University Council on Animal Care, Animal Use Subcommittee at Western University (Animal Use Protocol: 2010-040). Male Wistar rats ($n = 11$; Charles River Laboratories) aged 4-6 weeks and weighing 200-225 g were used. Rats were anesthetized with 5% isoflurane, maintained at 2% isoflurane (1 L/min oxygen) and placed into a stereotactic frame for cell implantation (Stoelting Co., IL, USA). Fur on the superior side of the head was removed to expose the skin prior to incision to mark the bregma, which is the area of the skull where the sagittal and coronal sutures joining the parietal and frontal bones meet. A burr hole was drilled 1-mm anterior and 3-mm right-lateral to the bregma. A micro-syringe (Hamilton 1700 series) containing 10^6 C6Luc cells suspended in 10 μ L of Hank's Buffered Salt Solution (HBSS) at 37°C was advanced to a depth of 4 mm in the brain. The cells were injected at a rate of 3 μ L/min. Bone wax was used to fill the burr hole to prevent cell suspension reflux. The incision was sutured and 1 mL of Meloxicam (5 mg/mL; Metacam, Boehringer Ingelheim Vetmedica, Ingelheim, Germany), a nonsteroidal anti-inflammatory drug, was administered by a subcutaneous injection. Each animal was imaged with BLI and mpMRI on days 4, 8, 11, 15 and 18 post-surgery. Prior to each imaging session, all animals had a tail vein catheter inserted and secured after being anesthetized with isoflurane.

2.2.5 Bioluminescence Imaging (BLI)

Anesthetized rats were given an intraperitoneal injection of D-Luciferin (150 mg/kg; PerkinElmer, Massachusetts, USA) and imaged on an IVIS Lumina XRMS In Vivo

Imaging System (PerkinElmer, Massachusetts, USA). To avoid imaging through the burr hole, animals were placed on their left side (tumour side closest to the camera) and images were collected for up to 30 minutes post-injection with the following parameters; exposure time = 1 min, binning factor = 8, f -number = 1, field of view = 12.5 cm.

2.2.6 Multiparametric Magnetic Resonance Imaging (mpMRI)

Animals were imaged on a 3 T MRI scanner (Discovery MR750 3.0 T, General Electric Healthcare, Illinois, USA). The heads of anesthetized rats were placed inside an eight-rung, 33-mm-inside-diameter bird cage radiofrequency (RF) coil (Morris Instruments Inc., Ontario, Canada), which was located within a custom-built insertable gradient coil (36). Each MRI session consisted of T_2 -weighted imaging, diffusion tensor imaging (DTI), and pre- and post-contrast enhanced (CE) T_1 -weighted imaging using gadolinium-DTPA (0.5 mmol/kg; Magnevist, Bayer, Leverkusen, Germany). 3D T_2 -weighted images were collected using a 3D fast spin-echo (CUBE, General Electric Healthcare, Illinois, USA) sequence with the following parameters: Repetition time (TR) = 4000 ms, echo time (TE) = 62 ms, echo train length (ETL) = 160, field of view (FOV) = 60×30×30 mm, acquisition matrix = 128×128×100, slice thickness = 0.6 mm, bandwidth = 62.5 kHz, and number of averages (NEX) = 9. DTI data were obtained using a 2D spin-echo single-slice echo-planar imaging sequence with the following parameters: TR = 6000 ms, TE = 71.1 ms, FOV = 60×60 mm, acquisition matrix = 120×120, 130 coronal slices, slice thickness = 3 mm, bandwidth = 166.7 kHz, NEX = 1, b -value = 1000 s/mm². Pre-CE ($n = 5$) and post-CE T_1 -weighted images were obtained using a 3D ultrafast gradient-recalled echo sequence for brain volume imaging (Fast GRE BRAVO, General Electric Healthcare, Illinois, USA)

with the following parameters: TR = 6.9 ms, TE = 2.9 ms, preparation time = 450 ms, FOV = 60×30×30 mm, acquisition matrix = 120×120×60, slice thickness = 0.5 mm, bandwidth = 62.50 kHz, NEX = 9, flip angle = 25°. Post-CE T_1 -weighted images were obtained 4 minutes after Gd-DTPA injection.

2.2.7 Image Analysis

For BLI, average radiance (photons/second/cm²/steradian) was measured using Living Image software by drawing a region-of-interest (ROI) over the head. For MRI, apparent diffusion coefficients (ADC) were calculated using a vendor-provided software analysis package for brain diffusion tensor imaging (Functool, General Electric Healthcare, Illinois, USA). Tumour volume measurements were obtained from T_2 -weighted and Post-Gd T_1 -weighted images using ITK-SNAP, a freeware image analysis tool (www.itksnap.org). Tumour boundaries, chosen based on post-contrast-enhanced (CE) T_1 -weighted images, were manually contoured in ITK-SNAP and tumour volumes were calculated. If non-contrast enhanced (NCE) regions were present within tumours, separate ROIs were drawn to measure CE and NCE tumour volumes. Histology images were co-registered to post-Gd T_1 -weighted MR images using 3D Slicer (Surgical Planning Laboratory, Harvard Medical School, Boston, Massachusetts) with a non-rigid, interactive, thin-plate spline extension by Gibson (37). Fiducial markers for the registration were placed within 3D Slicer on histological images and post-Gd T_1 -weighted MR images on identical morphological landmarks in the brain of the rat.

2.2.8 End-Point Histology

At end-point (18 days post-cell injection), animals were anesthetized with isoflurane and intravenously injected with pimonidazole (60 mg/kg; HypoxyProbe™-1; Hypoxyprobe Inc., Massachusetts, USA). After 30 minutes, animals were euthanized with an overdose of isoflurane followed by a 1-mL tail-vein injection of 1-M potassium chloride to ensure cardiac arrest. Each rat was pressure perfused with 4% paraformaldehyde (PFA) in phosphate buffer solution through the left ventricle. Following perfusion, the brain was excised and stored at 4°C in 4% PFA for an additional 24 hours. Brains were placed in solutions of progressively increasing glucose concentration (10%, 20% and 30% w/v) for 1 hour, 1 hour and 24 hours, respectively. Brains were then embedded in optimal cutting temperature compound and frozen at -80°C with a mixture of dry ice and methanol. Ten-micron sections were obtained on a microtome-cryostat (Leica CM1860, Wetzlar, Germany) and stained for the following: hematoxylin and eosin (H&E); 4',6-diamidino-2-phenylindole (DAPI); and hypoxia using the HypoxyProbe™-1 kit (Hypoxyprobe Inc., Massachusetts, USA). All whole brain histological images were obtained on an upright Zeiss Axio Imager Z1 (Carl Zeiss CG, Oberkochen, Germany), which included both bright field and fluorescence images. H&E, DAPI, green fluorescent protein (GFP), and hypoxia images were obtained.

2.2.9 Statistics

Statistical analyses were performed with the aid of a statistical analysis software known as GraphPad Prism v7 (GraphPad Software, Inc., California, USA). A one-way ANOVA and Tukey's *post hoc* test was performed for the cell doubling time. For most imaging

measurements over time, a one-way repeated measures ANOVA and Tukey's *post hoc* test was performed. A two-way repeated measures ANOVA and Sidak's *post hoc* test was performed to compare the ADC values between the CE and NCE groups over days 15 and 18. Pearson product-moment correlation and linear regression analyses were performed to identify any trends between any two given imaging measures. All statistical analyses were performed using a statistical value of $P = 0.05$.

2.3 Results

In vitro experiments were performed to evaluate the relationship between BLI signal intensity and cell number (Fig 2-2A/B), as well as the growth rates of C6Luc and naïve C6 cells (Fig 2-2C). A strong positive correlation was found between cell number and BLI signal (Fig 2-2A/B; $R^2 = 0.985$, $P < 0.05$; $n = 3$ for each group). No significant difference was detected between the doubling rates of C6 cells (11.9 ± 1.7 h), C6Luc cells (12.4 ± 1.7 h), and C6Luc cells incubated with D-Luc (10.3 ± 1.0 h) ($P = 0.801$).

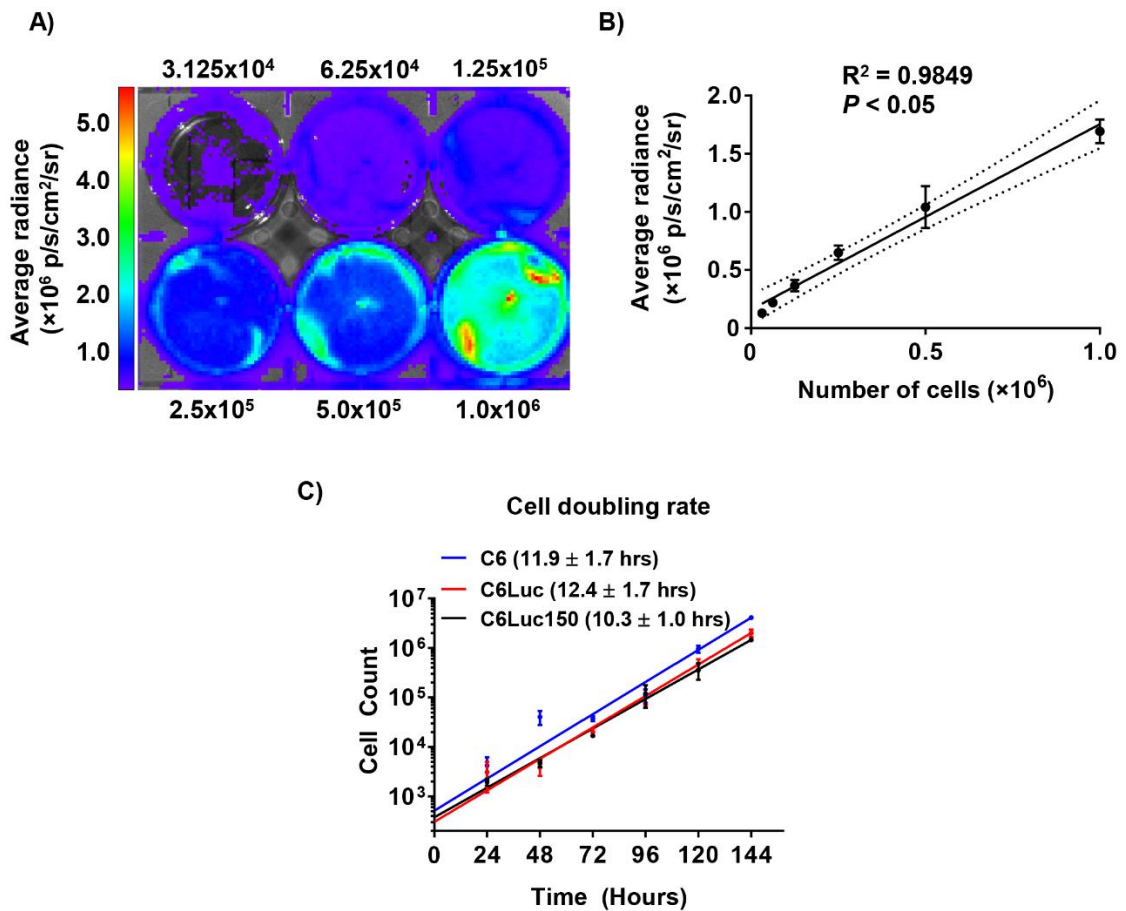


Figure 2-2. *In vitro* analysis of luciferase expression versus cell numbers, doubling rate, and luciferase activity over passage number.

A) Bioluminescence image overlaid on a bright field image of a six-well plate ($n = 3$) containing varying numbers of C6Luc cells, as shown. **B)** Image analysis showed a strong correlation between average radiance and the number of cells per well ($R^2 = 0.985$, $P < 0.05$). **C)** Doubling rates for non-transduced C6 glioma cells ($n = 6$), transduced C6Luc cells ($n = 6$), and C6Luc cells incubated with 150 μ g/mL of D-Luciferin ($n = 6$). No significant differences in doubling rates were noted.

A total of 11 Wistar rats were monitored with longitudinal BLI and mpMRI on days 4, 8, 11, 15 and 18 following intracranial implantation of C6Luc cells. During longitudinal

imaging, one rat was sacrificed prior to end-point due to a rapidly increasing tumour burden and deterioration of health; data from this animal was omitted. BLI images of a glioma-bearing rat are shown in Figure 2-3A. No significant changes in BLI signal were detectable across time (Figure 2-3B; $P > 0.05$). There were large variations in the magnitude of BLI signal across time when considering individual animals. Within 7 of the 11 of the rats, the average radiance peaked on or near day 11 (group average: $5.2 \pm 5.6 \times 10^5$ p/s/cm²/sr) and dropped two-fold by day 15 (group average: $2.1 \pm 2.3 \times 10^5$ p/s/cm²/sr) and nearly three-fold by day 18 (Fig 2-3C; pattern 1; group average: $1.9 \pm 2.4 \times 10^5$ p/s/cm²/sr). In contrast, for two rats, BLI signal increased gradually and plateaued around day 15 and 18 (Fig 2-3C; pattern 2); and for the final two animals, BLI signal slowly decreased after day 4 (Fig 2-3C; pattern 3).

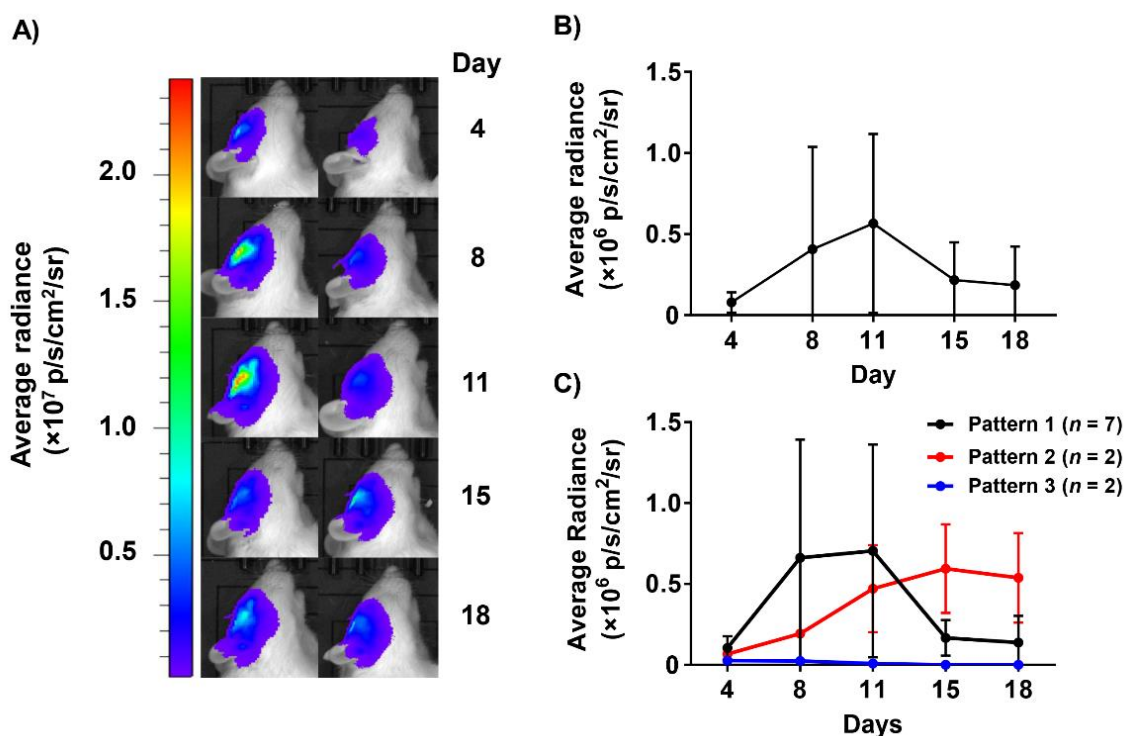


Figure 2-3. BLI of C6Luc orthotopic tumour growth in Wistar rats.

A) Bioluminescence images collected from days 4 to days 18 post-cell implantation. BLI images are overlaid on bright field images of a rat lying on its left side (tumour implanted in right side of brain). Left: Representative images of a rat where BLI signal increased from day 4 to day 11 followed by a drop in BLI signal on days 15 and 18. Right: Representative images of a rat where BLI signal steadily increased and plateaued. **B)** Due to large inter-subject variability, analysis of brain BLI signal (average radiance) revealed no significant changes with respect to time ($P > 0.05$). **C)** The three BLI patterns observed between individual animals. Data are presented as mean \pm SD.

We noted qualitative morphological differences in brain and tumour MR features across animals. Nine rats displayed tissue damage from the needle tract during injection until endpoint, and seven rodents displayed defined tumour boundaries. One rat displayed evidence

of a hemorrhage on day 11 based on T_2 -weighted MRI but recovered by day 18 (not shown in this thesis). Tumour volumes were measured on both T_2 -weighted and post-CE T_1 -weighted MR images (Fig 2-4A). Based on T_2 -weighted MRI, eight rodents had tumours that monotonically increased to an average volume of $275 \pm 175 \text{ mm}^3$ by day 18. Two rodents displayed a decrease in tumour volume from day 15 to day 18, and 2 rodents had tumour volumes that decreased continually after day 11. Total tumour volume based on T_2 -weighted MRI significantly increased from $11 \pm 9 \text{ mm}^3$ on day 4 to $215 \pm 126 \text{ mm}^3$ on day 15 (Fig 2-4B; $P < 0.05$). No significant change in tumour volume were observed from day 15 to day 18 ($P = 0.230$).

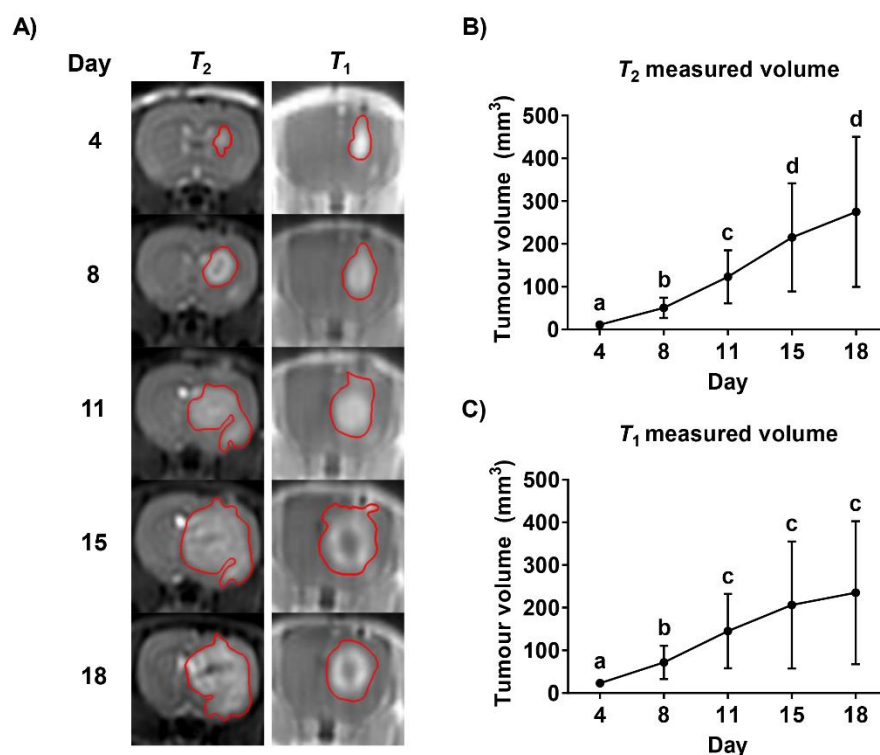


Figure 2-4. Representative longitudinal post-Gd T_1 - and T_2 -weighted MRI of C6Luc tumour growth.

A) T_2 -weighted images (left) and post-Gd T_1 -weighted (right) MRI of a representative animal brain showing continued tumour growth over time. Tumours were manually contoured (red) and total T_2 (**B**) and T_1 (**C**) tumour volume over time was determined ($n = 11$ rats). The letters, a, b, c and d, denote significant differences across time points ($P < 0.05$). Data are presented as mean \pm SD.

Similar to T_2 -weighted images, five rodents displayed increasing post-CE T_1 -weighted tumour volume from 23.3 ± 9.80 mm³ on day 4 to 235 ± 168 mm³ on day 18. Three rodents peaked in tumour volume on day 15 and decreased on day 18, two rodents had decreasing

tumour volume past day 11 and one rodent had a decrease in tumour volume on day 15, but rapidly increased by day 18. Post-CE T_1 -weighted tumour volumes exhibited a statistically significant increase from $23 \pm 10 \text{ mm}^3$ on day 4 to $145 \pm 87 \text{ mm}^3$ on day 11 (Fig 2-4C; $n = 11$; $P < 0.05$). No significant changes in post-CE T_1 -weighted tumour volumes were observed between day 11 and 18 ($P = 0.230$).

Post-CE T_1 - and T_2 -weighted tumour volumes had a strong positive correlation (Fig 2-5A; $R^2 = 0.884$, $P < 0.05$). In contrast, when all five longitudinal imaging time points were considered, T_2 -weighted tumour volumes were not significantly correlated to BLI signal (Fig 2-5B; $R^2 = 0.027$, $P = 0.226$) and post-CE T_1 -weighted tumour volumes were poorly correlated to BLI signal (Fig 2-5C; $R^2 = 0.074$, $P < 0.05$). To further investigate the relationship between total tumour volume and BLI signal, T_1 - and T_2 -weighted tumour volume data from days 4 to 11 were compared to BLI signal on those days. Both T_1 and T_2 tumour volumes were moderately correlated to BLI signal when considering only days 4 to 11 (Fig 2-5D; $R^2 = 0.305$, $P < 0.05$; Fig 2-5E; $R^2 = 0.237$, $P < 0.05$), suggesting a relationship in tumour volume and BLI signal during early, but not late, tumour progression (*i.e.*, beyond day 11).

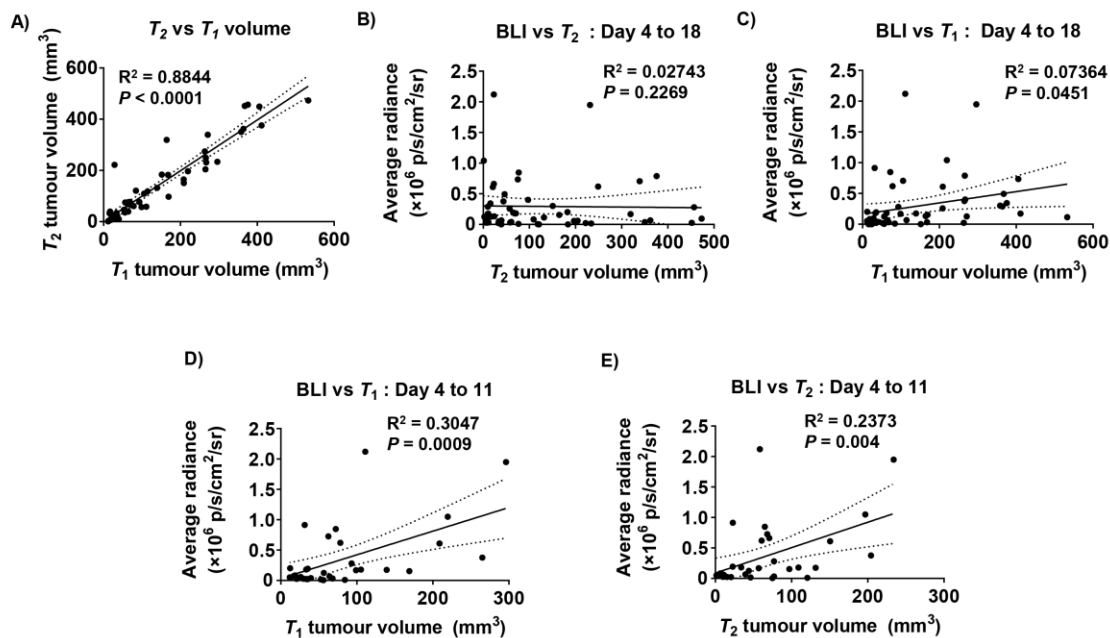


Figure 2-5. Correlational plots of total T_2 and post-Gd T_1 tumour volume to BLI signal.

A) Post-Gd T_1 -weighted tumour volume was strongly correlated to T_2 -weighted tumour volume. **B)** T_2 tumour volume was not correlated to BLI signal across all imaging days (4 to 18). **C)** T_1 tumour volume was poorly correlated to BLI signal across all imaging days (4 to 18). **D)** T_1 tumour volume was moderately correlated to BLI for data from days 4 to 11 only. **E)** T_2 tumour volume was moderately correlated to BLI for data from days 4 to 11 only. Day 15 and 18 were excluded due to the formation of a NCE region. The line of best fit and the 95% confidence interval was plotted for each graph.

Beyond day 11, we noted in post-CE T_1 -weighted MR images that there were foci within some tumours, primarily within the core, which did not appear to enhance. Therefore, we separately measured the contrast enhanced (CE) and non-contrast-enhanced (NCE) tumour volumes to evaluate whether these measurements correlated with BLI signal beyond day 11. One rodent displayed hypo-intense regions within the tumour in post-CE T_1 -weighted MRI on day 8 but it was not possible to differentiate between tissue damage due to the

needle tract or lack of contrast agent; therefore, this animal was excluded from data analyses. Two of the seven rodents did not have a NCE region on day 11 and it was likely that these NCE regions on day 11 were due to tissue damage from the surgery needle, therefore this day was excluded from analyses. It is impossible to perform a repeated measures ANOVA without extrapolating the data for day 11. In addition, these NCE regions were superficial and was associated with the tissue damage from stereotactic surgery. Seven of the 11 rodents displayed a NCE region surrounded by a CE region within the tumour on days 15 and 18, and a representative rodent is shown in Figure 2-6A. CE tumour volume significantly increased from $23 \pm 10 \text{ mm}^3$ on day 4 to $143 \pm 85 \text{ mm}^3$ on day 11 (Fig 2-6B; $P < 0.05$). No significant changes in CE tumour volume were observed from days 11 to 18 ($P > 0.05$). NCE tumour volume was not significantly different between days 15 and 18 (Fig 2-6C; $P = 0.119$). The relationship between CE tumour volume and BLI signal was examined to determine if perfusion solely accounted for the lack of correlation between total tumour volume and BLI signal; however, CE tumour volume was poorly correlated to BLI signal (Fig 2-6D; $R^2 = 0.088$, $P < 0.05$).

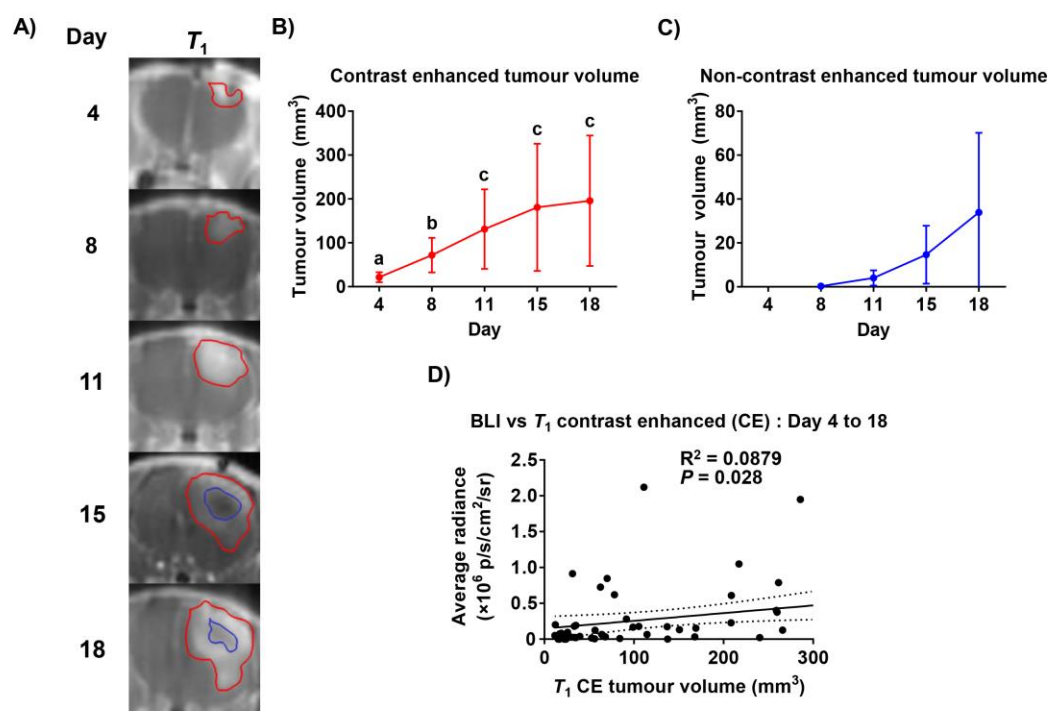


Figure 2-6. Longitudinal post-Gd T_1 -weighted MRI with CE and NCE regions differentiated and examined for correlation.

A) Representative post-Gd T_1 -weighted MR images of a representative rat with CE and NCE regions contoured in red and blue, respectively. **B)** CE tumour volume significantly increased over time, whereas NCE tumour volume (**C**) did not significantly change from day 15 and 18. **D)** T_1 CE tumour volume was slightly more correlated to BLI signal when compared to T_1 tumour volume, but still had a very poor correlation. The line of best fit and the 95% confidence interval was plotted. Significantly different groups are denoted by the letters, a, b, and c. All data are shown as mean \pm SD.

To evaluate water diffusivity within tumours as a measure of cellularity, we performed DTI of rats over time (Fig 2-7A). An ADC map and matched post-CE T_1 -weighted MR images of a representative animal, with CE and NCE regions contoured, are shown in Figure 2-

7A. On day 4, there was large variability in ADC values, which was presumably due to tissue damage from the needle tract during stereotactic surgery. Whole tumour ADC values significantly increased from days 8 and 11 to day 18 (Fig 2-7B; $P < 0.05$). Of the 7 rodents that displayed NCE regions within tumours at day 15 and 18, the ADC values within these NCE regions were significantly higher than in CE regions (Fig 2-7C; $P < 0.05$).

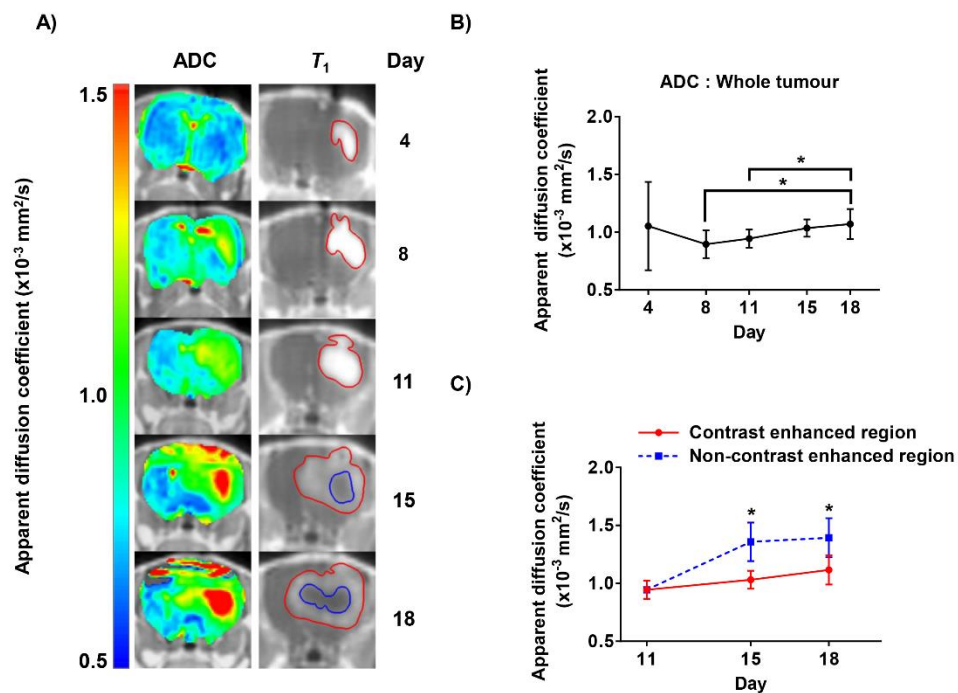


Figure 2-7. Longitudinal apparent diffusion coefficient (ADC) maps and post-Gd T_1 -weighted MRI with their respective plots.

A) ADC maps (left) overlaid on T_1 -weighted MR images with CE (red) and NCE (blue) ROIs contoured (right). **B)** ADC values over the whole contoured (red) tumour plotted against time. Whole-tumour ADC values significantly increased on day 18 when compared to days 8 and 11. **C)** ADC values within NCE or CE regions plotted with respect to time.

ADC values within NCE regions were significantly increased on both day 15 and 18 when compared to ADC values in CE regions. * denotes significant differences at $P < 0.05$. All data are shown as mean \pm SD.

At end-point, qualitative assessment of co-registered H&E microscopy images and post-gd T_1 -weighted MRI demonstrated that large regions of tissue lacking nuclei or cytoplasmic proteins within tumour tissue (Fig 2-8; H&E) corresponded to areas of non-contrast enhancement (Fig 2-8; Post-Gd T_1). Co-registered DAPI images (Fig 2-8; DAPI) show nuclei staining, which corresponds to the presence of nuclei from H&E staining. Results from DAPI staining are similar to H&E; there are many nuclei in peripheral tumour tissue, and a lack of nuclei near the centre of the tumour mass. GFP is co-expressed with Luc, therefore GFP microscopy (Fig 2-8; GFP) displayed cells (*i.e.* C6Luc) that were actively transcribing and translating the GFP and Luc genes at end-point. GFP is detectable within regions of viable tumour tissue (which correspond to areas where tumour nuclei are present), but undetectable in regions that lack nuclei. Very low levels of GFP could be detected in Fig 8, rows #3 and #4, despite the presence of intact tumour tissue. Hypoxia staining (Fig 2-8; Hypoxia) demonstrated regional hypoxia within the tumour. There are few regions of hypoxia, predominately within the tumour and adjacent to regions lacking nuclei within the tumour. DAPI, GFP and hypoxia were overlaid (Fig 2-8; DAPI GFP Hypoxia) to demonstrate areas of GFP were coincidental with DAPI and to provide contrast to hypoxia staining to identify morphological features. Co-registered ADC maps (Fig 2-8; ADC) show regions of increased ADC values which correspond to NCE regions on post-Gd T_1 -weighted MR images and to the extracellular matrix and empty regions on histology.

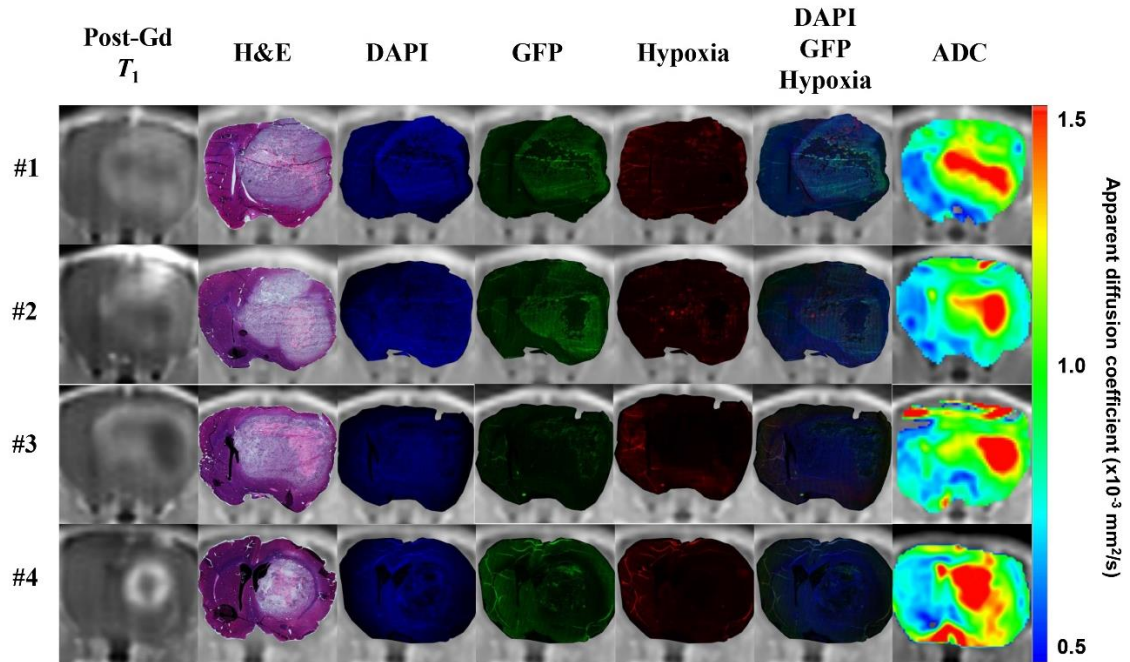


Figure 2-8. Fully co-registered whole brain histology, which includes H&E, DAPI, GFP and hypoxia, to post-Gd T_1 -weighted MR images with the respective co-registered ADC maps of four representative animals.

A) Post-Gd T_1 -weighted MRI shows NCE and CE regions, and was the reference image for non-rigid transformation. Hematoxylin stains for positively charged structures (*i.e.* nuclei). Eosin stains for negatively charged structures that can be found within the cell (*i.e.* compounds and proteins commonly found in the cytoplasm). DAPI is a fluorescent dye that binds to A-T rich regions in DNA (*i.e.* nuclei). GFP is co-expressed with Luc, therefore only active, live cells can transcribe the gene and express the protein. Hypoxyprobe™ (pimonidazole) stains for hypoxic regions, where the pimonidazole binds to thiol-containing proteins in hypoxic cells. DAPI, GFP and hypoxia images were overlaid. Respective ADC maps of each animal demonstrated an increased in ADC values within NCE regions.

2.4 Discussion

In this study, we present the first use of combined BLI and mpMRI to quantitatively characterize orthotopic C6 tumour growth in rats, a well-documented model of glioma (14, 15, 38). The combination of these two imaging modalities allowed complementary assessment of multiple tumour growth characteristics, including total tumour volume, CE and NCE tumour volume, ADC measures for whole tumour, CE and NCE regions, as well as relative cellular viability using BLI. Conventional MRI, which includes post-CE T_1 - and T_2 -weighted MRI, is an excellent non-invasive imaging tool to longitudinally assess morphological changes in the brain. However, conventional MRI is mainly limited to morphological and functional information, and, unlike BLI, does not directly measure the viability of cells over time in rat models. An added benefit of using BLI is that it can sensitively detect changes in tumour viability prior to any changes in tumour burden because morphological changes are slow to occur when compared to molecular changes. Unfortunately, BLI provides little anatomical information and spatial information is degraded by light scatter through tissue and the skull. Thus, a combination of both mpMRI and BLI may overcome the limitations of each individual modality and provide morphological, functional and molecular information about tumour growth in this rat model.

Our imaging results indicated that MR measurements of tumour volume did not correlate with BLI signal beyond day 11 (Fig 2-5). This highlights the complementary nature of our imaging approach as new information is provided with BLI that is not attainable with conventional MRI measures of tumour burden. Previous studies have reported a linear

relationship between tumour volume and BLI signal for glioma models (31, 39-42). However, other studies have reported similar findings as this study; observing a lack of a relationship between tumour volume and BLI signal, particularly at later time points when tumour cores can become ill-perfused and/or necrotic. Jost *et al.* reported a small subset of animals ($n = 2$) demonstrating decreased BLI signal despite increasing tumour volume and attributed it to hemorrhage and necrosis (31). Likewise, Rehemtulla *et al.* support these findings, and concluded that BLI signal was less correlated to MRI measurements with necrotic tumours in the case of treated tumours or large untreated tumours (32).

In support of the evidence presented by Jost *et al.* (31) and Rehemtulla *et al.* (32), regions that did not enhance on post-Gd T_1 -weighted MRI (NCE regions) became apparent beyond day 11, the time point after which BLI signal decreased in the majority of animals, and these corresponded to regions of significantly increased ADC values from diffusion weighted imaging (DWI). DWI is a functional MRI technique that is sensitive to small changes within tissue and has become a useful tool to characterize brain tissue cellularity. Sugahara *et al.* has previously described the inverse relationship between tumour cellularity and apparent diffusion coefficient (ADC) values (43). An increase in tissue cellularity would restrict the movement or diffusion of water molecules and vice versa. Previous studies have described this relationship between cellularity and tumour necrosis (44-46). Tumour cellularity assessed by ADC measurements decreased significantly over time (Fig 2-7B). Tumour cellularity has been reported to decrease in the event of edema, hemorrhage, and necrosis among other factors (23, 26, 47). Edema and hemorrhage has been ruled out as potential causes of decreased tumour cellularity because edema appears as hyper-intense and hemorrhage appears as hypo-intense signals in T_2 -weighted MRI, both

of which were not present in this study when T_2 -weighted MR images were examined. NCE regions within the tumour had significantly increased ADC values when compared to CE regions on days 15 and 18 (Fig 2-7C). Moreover, our co-registered end-point whole brain immunohistochemistry provided qualitative evidence to further strengthen this finding. Microscopy analysis of H&E stained sections allowed specific features to be differentiated when comparing healthy brain tissue and tumour tissue, such as tumour tissue pattern, and focal areas of necrosis (48). H&E staining showed regions of necrosis within the tumour that corresponded to NCE regions and regions of high ADC values (Fig 2-8). In addition, DAPI images demonstrate that there were very few nuclei in regions identified as necrotic in H&E images, NCE regions and regions of high ADC values. The C6 tumour cells co-expressed GFP and red-shifted *Luciola Italicia* luciferase; no GFP signal was detected within these necrotic regions based on GFP microscopy images. In two cases, we found very little detectable GFP signal within CE and NCE regions of very large tumours as seen in rows #3 and #4 in Figure 2-8. Overall, our findings supported previous findings in literature and the presence of necrosis in the C6 rat model as the main contributor to the decrease in BLI signal in a majority of the animals,

Brutkiewicz *et al.* reported similar findings to this study but attributed the discordance of BLI signal and MRI metrics to the luciferase-luciferin reaction impeding tumour growth in high luciferase expressing cell lines (49). Contrary to this, our study has demonstrated *in vitro* that D-luciferin incubation had no significant effect on growth rate of C6Luc tumour cells (Fig 2-2C). Zhao *et al.* had previously described that BLI signal may be restricted due to limited delivery of BLI substrate to the tumour (50). The lack of Gd-DTPA uptake and decreased cellularity strongly suggested that these tumours have developed an

ill-perfused necrotic core, which was not uncommon of GBM as previously described in literature (51, 52). However, Doblus *et al.* states that gadolinium is not a specific, direct measure of angiogenesis nor perfusion, and only reflects an impacted BBB (16). Thus, having a direct measure of perfusion, such as PWI, would have been a powerful measurement to rule out limited substrate delivery or limited vascularization.

Khalil *et al.* has reported that hypoxic regions within the tumour may have a negative influence on BLI signal due to the inherent requirement of oxygen in the luciferin-luciferase reaction (53). We found small regions of hypoxia, which were predominately adjacent to necrotic regions, present within tumours based on immunohistochemistry (Fig 2-8; #1 and #2). There were two cases where hypoxia was undetectable within both CE and NCE regions of the tumour despite large tumours with necrosis present (Fig 2-8; #3 and #4). This qualitative assessment supported previous findings in literature, as hypoxia was present within the tumour which can limit the luciferase-luciferin chemical reaction. However, it is unlikely the primary cause of the three-fold decrease in BLI signal due to the lack of hypoxia staining.

We propose that all these factors (necrosis, hypoxia, and limited substrate delivery) are contributors to the decreased BLI signal we see in our study at later time points in the majority of animals. In addition, these three factors are all related. The lack of vascularization to certain regions of the tumour may limit blood and oxygen delivery causing these regions to become hypoxic, which would eventually become necrotic, due to a mismatch of metabolic supply and demand (54, 55). The increased metabolism of tumour cells (56) which leads to the lack of oxygen and adenosine triphosphate (ATP) creates a difficult environment for the luciferin-luciferase reaction to go to completion because this

BLI reaction requires both ATP and oxygen as co-factors. The increased metabolism of tumour cells, decreased oxygen and ATP availability, limited vascularization within the tumour limits D-luciferin availability, preventing the luciferase-luciferin pathway from producing detectable light (50).

As mentioned previously, mpMRI metrics (NCE and high ADC regions) correspond to areas of necrosis as determined in immunohistochemistry (Fig 2-8). Therefore, it can be qualitatively concluded that *in vivo* imaging can accurately recapitulate and provide information on real morphological changes, evident in post-mortem histology. It can be inferred that NCE regions on day 11 and 15 are likely signs of early-necrosis. Thus, we can non-invasively monitor the tumour and identify growth characteristics such as the formation of necrosis. In further support of this particular inference, functional imaging provided another metric, cellularity, which can be related to the formation of a necrotic core. Interestingly, the lack of correlation between mpMRI and BLI measurements highlighted the importance of having an independent measurement of tumour viability on a molecular level. We have shown here that BLI provides an important measure unobtainable in mpMRI, which is cellular viability. We have shown in this study that BLI signal tended to decrease after day 11, in which areas of NCE or necrosis began to form. BLI is sensitive to changes in cellular viability and was able to detect a change in viability before any apparent anatomical changes were present.

Our study highlights the large variability of disease progression across animals in this model. For instance, two rodents displayed slowly increasing BLI signal over time, with some decline on day 18 despite increasing tumour volumes. This is important information and suggests investigating each animal on an individual basis with both BLI and MRI when

moving forward with the assessment of tumour response to treatment. It would be naïve to assume that all tumours would respond identically when given the same therapy regimen. Therefore, the imaging and monitoring of tumour progression and response to treatment needs to occur on a per animal basis when attempting to deliver or assess the efficacy of a certain therapeutic plan. Another very important point to mention is the current method to assess tumour growth characteristics and response to therapy, which is through morphological changes in tumour volume as seen in mpMRI, has its limitations and may not be the most sensitive method when used alone in this model. The evaluation of treatment response based only on tumour volume is inherently flawed, as change is slow to occur and provides no information on the cellular viability of cancer cells. As this study has shown, the biology and cellular viability within the tumour was evolving considerably over time. It is likely that the evaluation of treatment response may be inaccurate in this model when the only metric for response is tumour volume. This study has highlighted the complementary value of using both BLI and mpMRI and would prove beneficial to future studies addressing the evaluation of treatment response in this model.

A limitation of this study is the lack of histological samples obtained at each time point from different cohorts of animals. Evaluation of this tissue could help confirm the development of hypoxia, necrosis or lack of perfusion and help explain the imaging measures obtained with BLI and mpMRI over time. Alternatively, the use of other molecular imaging tools to identify and measure tumour growth characteristics would provide a deeper understanding of the various biological mechanisms occurring within the tumour during progression in this rat model. Some examples are ^{18}F -fluodeoxyglucose (^{18}F -FDG), which enables metabolic imaging of the tumour through glucose activity, ^{18}F -

fluoromisonodazole (^{18}F -FMISO), which probes regional hypoxia independent of BBB disruption and lack of perfusion, and ^{18}F - galacto-arginine-glycine-aspartic acid (^{18}F -galacto-RGD), which is a probe for angiogenesis (57). Another imaging modality that would be useful to improve the ability to describe tumour progression and treatment response is ^1H magnetic resonance spectroscopy (MRS). ^1H MRS can measure various metabolites (*e.g.* N-acetyl aspartate, choline, and creatine) non-invasively which may aid in treatment planning and assessment (58). Expanding on MRS, is a novel imaging technique referred to as HP ^{13}C MRSI. HP ^{13}C -pyruvate MRSI is a metabolic imaging modality that measures the conversion of pyruvate to lactate, which provides information of metabolism (59). The imaging of metabolism with ^{18}F -FDG PET or HP ^{13}C -pyruvate MRSI provides a method to monitor the biological activity of the tumour, which can be a useful surrogate measure of treatment response (60, 61). PET-MRI allows for co-registered PET molecular imaging to MR anatomical images, which opens a window of opportunity to delineate these various biological features, that include necrosis, hypoxia and angiogenesis, of GBM in this model.

Knowledge of the tumour microenvironment, its biology and characteristics of natural progression should be included in interpretation of imaging data used to assess treatment response. For example, if one was assessing novel therapies in the C6Luc GBM rodent model using mpMRI and BLI and applied treatment near day 11, one could wrongly assume that therapy was effective because BLI signal dropped on days 15 and 18, when in fact, the decrease in BLI signal is often seen in untreated tumours. It will be very interesting to apply this multimodality imaging framework to evaluate tumour characteristics and eventually novel therapies in genetically engineered mice (GEM) or patient derived

xenograft (PDX) glioma models. PDXs are becoming more prevalent in this research field because they have shown to be highly reflective of human GBM and have been used for assessing treatment response in mice (62). This assessment of treatment response has been shown to have strong correlation to predicting clinical response.

In conclusion, this was the first longitudinal study to apply a multimodality imaging framework, mpMRI and BLI, in an orthotopic C6Luc rodent model to characterize the natural progression of GBM. This study also applied whole brain histological imaging that was co-registered to post-Gd T_1 -weighted MR images to qualitatively assess the correlation between *in vivo* imaging metrics to end-point histology. This study highlighted the importance of having an independent measure of tumour cell viability because assessment based solely on tumour volumes from MRI was not reliable and did not truly reflect the nature of GBM in each animal. Changes were slow to occur in MRI, for example, in BLI, a decrease in tumour viability was detected by day 11 to 15, whereas metrics of tumour burden in mpMRI suggested a possible decrease in tumour viability (due to the presence of a necrotic core) by day 15 to 18. In addition, it is difficult to conclude that these NCE regions correspond to necrotic regions without additional imaging techniques or histology, as Gd-DTPA is non-specific and reliant on contrast agent delivery. BLI and mpMRI showed positive correlation on the initial time points, but diverged on days 15 and 18. Further investigation was warranted and three new main hypotheses were developed, a lack of substrate delivery or perfusion, the presence of hypoxia and the formation of necrosis within the tumour. This study has provided evidence for the presence of necrosis, which contributed to the decrease in BLI signal as qualitatively confirmed through DWI and histology. This study highlights the difficulties in evaluating treatment response through

non-invasive imaging in the C6Luc rat model. Future studies should include multimodality imaging to provide a greater understanding of the disease model and obtain as many independent metrics of tumour response as practical for accurate assessment. There are many promising animal models that this imaging framework could be applied to. An in-depth imaging analyses of such models during progression may provide new insights to further improve clinical treatments and outcomes.

2.5 References

1. Canadian Cancer Society. Canadian Cancer Society's Advisory Committee on Cancer Statistics. Canadian Cancer Statistics 2017. 2017.
2. Ostrom QT, Gittleman H, de Blank PM, Finlay JL, Gurney JG, McKean-Cowdin R, et al. American Brain Tumor Association Adolescent and Young Adult Primary Brain and Central Nervous System Tumors Diagnosed in the United States in 2008-2012. *Neuro Oncol.* 2016;18 Suppl 1:i1-i50.
3. Parsons DW, Jones S, Zhang X, Lin JC, Leary RJ, Angenendt P, et al. An integrated genomic analysis of human glioblastoma multiforme. *Science.* 2008;321(5897):1807-12.
4. Luwor RB, Stylli SS, Kaye AH. Using bioluminescence imaging in glioma research. *J Clin Neurosci.* 2015;22(5):779-84.
5. Nitta T SK. Prognostic implications of the extent of surgical resection in patients with intracranial malignant gliomas. *Cancer.* 1995;75(11):2727-31.
6. Laperriere N, Zuraw, L., Cairncross, G. Radiotherapy for newly diagnosed malignant glioma in adults: a systematic review. *Radiotherapy and Oncology.* 2002;64(3):259-73.
7. Walker MD, Green SB, Byar DP, Alexander EJ, Batzdorf U, Brooks WH, et al. Randomized Comparisons of Radiotherapy and Nitrosoureas for the Treatment of Malignant Glioma after Surgery. *New England Journal of Medicine.* 1980;303(23):1323-9.
8. Galli R, Binda E, Orfanelli U, Cipelletti B, Gritti A, De Vitis S, et al. Isolation and characterization of tumorigenic, stem-like neural precursors from human glioblastoma. *Cancer Res.* 2004;64(19):7011-21.
9. Chicoine MR, Silbergeld DL. Invading C6 glioma cells maintaining tumorigenicity. *J Neurosurg.* 1995;83(4):665-71.

10. Giese A, Bjerkvig R, Berens ME, Westphal M. Cost of migration: invasion of malignant gliomas and implications for treatment. *J Clin Oncol*. 2003;21(8):1624-36.
11. Hanahan D, Weinberg RA. The hallmarks of cancer. *Cell*. 2000;100(1):57-70.
12. Plate KH, Risau W. Angiogenesis in malignant gliomas. *Glia*. 1995;15(3):339-47.
13. Kao HW, Chiang SW, Chung HW, Tsai FY, Chen CY. Advanced MR imaging of gliomas: an update. *Biomed Res Int*. 2013;2013:970586.
14. Barth RF, Kaur B. Rat brain tumor models in experimental neuro-oncology: the C6, 9L, T9, RG2, F98, BT4C, RT-2 and CNS-1 gliomas. *J Neurooncol*. 2009;94(3):299-312.
15. Jacobs VL, Valdes PA, Hickey WF, De Leo JA. Current review of in vivo GBM rodent models: emphasis on the CNS-1 tumour model. *ASN Neuro*. 2011;3(3):e00063.
16. Doblaz S, Saunders D, Kshirsagar P, Pye Q, Oblander J, Gordon B, et al. Phenyl-tert-butyl nitron induces tumor regression and decreases angiogenesis in a C6 rat glioma model. *Free Radic Biol Med*. 2008;44(1):63-72.
17. Sheehan J, Ionescu A, Pouratian N, Hamilton DK, Schlesinger D, Oskouian RJ, Jr., et al. Use of trans sodium crocetin for sensitizing glioblastoma multiforme to radiation: laboratory investigation. *J Neurosurg*. 2008;108(5):972-8.
18. Tanriover N, Ulu MO, Sanus GZ, Bilir A, Canbeyli R, Oz B, et al. The effects of systemic and intratumoral interleukin-12 treatment in C6 rat glioma model. *Neurol Res*. 2008;30(5):511-7.
19. Benda P, Lightbody J, Sato G, Levine L, Sweet W. Differentiated rat glial cell strain in tissue culture. *Science*. 1968;161(3839):370-1.
20. Schmidek HH, Nielsen SL, Schiller AL, Messer J. Morphological studies of rat brain tumors induced by N-nitrosomethylurea. *J Neurosurg*. 1971;34(3):335-40.
21. Stokes AM, Hart CP, Quarles CC. Hypoxia Imaging With PET Correlates With Antitumor Activity of the Hypoxia-Activated Prodrug Evofosfamide (TH-302) in Rodent Glioma Models. *Tomography*. 2016;2(3):229-37.
22. Qi Q, Yeung TP, Lee TY, Bauman G, Crukley C, Morrison L, et al. Evaluation of CT Perfusion Biomarkers of Tumor Hypoxia. *PLoS One*. 2016;11(4):e0153569.
23. Yao NW, Chang C, Lin HT, Yen CT, Chen JY. Functional assessment of glioma pathogenesis by in vivo multi-parametric magnetic resonance imaging and in vitro analyses. *Sci Rep*. 2016;6:26050.
24. Weller M, Cloughesy T, Perry JR, Wick W. Standards of care for treatment of recurrent glioblastoma--are we there yet? *Neuro Oncol*. 2013;15(1):4-27.

25. Mabray MC, Barajas RF, Jr., Cha S. Modern brain tumor imaging. *Brain Tumor Res Treat.* 2015;3(1):8-23.
26. Perez-Carro R, Cauli O, Lopez-Larrubia P. Multiparametric magnetic resonance in the assessment of the gender differences in a high-grade glioma rat model. *EJNMMI Res.* 2014;4(1):44.
27. Garteiser P, Doblas S, Watanabe Y, Saunders D, Hoyle J, Lerner M, et al. Multiparametric assessment of the anti-glioma properties of OKN007 by magnetic resonance imaging. *J Magn Reson Imaging.* 2010;31(4):796-806.
28. Boulton JK, Walker-Samuel S, Jamin Y, Leiper JM, Whitley GS, Robinson SP. Active site mutant dimethylarginine dimethylaminohydrolase 1 expression confers an intermediate tumour phenotype in C6 gliomas. *J Pathol.* 2011;225(3):344-52.
29. Liao J, Xia R, Liu T, Feng H, Ai H, Song B, et al. In vivo dynamic monitoring of the biological behavior of labeled C6 glioma by MRI. *Mol Med Rep.* 2013;7(5):1397-402.
30. Contag CH, Ross BD. It's not just about anatomy: in vivo bioluminescence imaging as an eyepiece into biology. *J Magn Reson Imaging.* 2002;16(4):378-87.
31. Jost SC, Collins L, Travers S, Piwnica-Worms D, Garbow JR. Measuring brain tumor growth: combined bioluminescence imaging-magnetic resonance imaging strategy. *Mol Imaging.* 2009;8(5):245-53.
32. Rehemtulla A, Stegman LD, Cardozo SJ, Gupta S, Hall DE, Contag CH, et al. Rapid and quantitative assessment of cancer treatment response using in vivo bioluminescence imaging. *Neoplasia.* 2000;2(6):491-5.
33. Xi G, Rajaram V, Mania-Farnell B, Mayanil CS, Soares MB, Tomita T, et al. Efficacy of vincristine administered via convection-enhanced delivery in a rodent brainstem tumor model documented by bioluminescence imaging. *Childs Nerv Syst.* 2012;28(4):565-74.
34. Hwang DW, Ko HY, Lee JH, Kang H, Ryu SH, Song IC, et al. A nucleolin-targeted multimodal nanoparticle imaging probe for tracking cancer cells using an aptamer. *J Nucl Med.* 2010;51(1):98-105.
35. Boulton JK, Terkelsen J, Walker-Samuel S, Bradley DP, Robinson SP. A multiparametric imaging investigation of the response of C6 glioma xenografts to MLN0518 (tandutinib) treatment. *PLoS One.* 2013;8(4):e63024.
36. Foster-Gareau P, Heyn C, Alejski A, Rutt BK. Imaging single mammalian cells with a 1.5 T clinical MRI scanner. *Magn Reson Med.* 2003;49(5):968-71.
37. Gibson E. 3D fusion of histology to multi-parametric MRI for prostate cancer imaging evaluation and lesion-targeted treatment planning. 2014.

38. Grobбен B, De Deyn PP, Slegers H. Rat C6 glioma as experimental model system for the study of glioblastoma growth and invasion. *Cell Tissue Res.* 2002;310(3):257-70.
39. Parkins KM, Hamilton AM, Makela AV, Chen Y, Foster PJ, Ronald JA. A multimodality imaging model to track viable breast cancer cells from single arrest to metastasis in the mouse brain. *Sci Rep.* 2016;6:35889.
40. Baumann BC, Dorsey JF, Benci JL, Joh DY, Kao GD. Stereotactic intracranial implantation and in vivo bioluminescent imaging of tumor xenografts in a mouse model system of glioblastoma multiforme. *J Vis Exp.* 2012(67).
41. Ramasawmy R, Johnson SP, Roberts TA, Stuckey DJ, David AL, Pedley RB, et al. Monitoring the Growth of an Orthotopic Tumour Xenograft Model: Multi-Modal Imaging Assessment with Benchtop MRI (1T), High-Field MRI (9.4T), Ultrasound and Bioluminescence. *PLoS One.* 2016;11(5):e0156162.
42. Genevois C, Loiseau H, Couillaud F. In Vivo Follow-up of Brain Tumor Growth via Bioluminescence Imaging and Fluorescence Tomography. *Int J Mol Sci.* 2016;17(11).
43. Sugahara T, Korogi Y, Kochi M, Ikushima I, Shigematu Y, Hirai T, et al. Usefulness of diffusion-weighted MRI with echo-planar technique in the evaluation of cellularity in gliomas. *J Magn Reson Imaging.* 1999;9(1):53-60.
44. Chawla S, Kim S, Wang S, Poptani H. Diffusion-weighted imaging in head and neck cancers. *Future Oncol.* 2009;5(7):959-75.
45. White NS, McDonald C, Farid N, Kuperman J, Karow D, Schenker-Ahmed NM, et al. Diffusion-weighted imaging in cancer: physical foundations and applications of restriction spectrum imaging. *Cancer Res.* 2014;74(17):4638-52.
46. Holodny AI, Ollenschlager M. Diffusion imaging in brain tumors. *Neuroimaging Clin N Am.* 2002;12(1):107-24, x.
47. Asanuma T, Doblaz S, Tesiram YA, Saunders D, Cranford R, Pearson J, et al. Diffusion tensor imaging and fiber tractography of C6 rat glioma. *J Magn Reson Imaging.* 2008;28(3):566-73.
48. Madabhushi V, Venkata R, Garikaparthi S, Kakarala S, Duttaluru S. Role of immunohistochemistry in diagnosis of brain tumors: A single institutional experience. *J NTR Univ Health Sci.* 2015;4(2):103-11.
49. Brutkiewicz S, Mendonca M, Stantz K, Comerford K, Bigsby R, Hutchins G, et al. The expression level of luciferase within tumour cells can alter tumour growth upon in vivo bioluminescence imaging. *Luminescence.* 2007;22(3):221-8.
50. Zhao D, Richer E, Antich PP, Mason RP. Antivascular effects of combretastatin A4 phosphate in breast cancer xenograft assessed using dynamic bioluminescence imaging and confirmed by MRI. *FASEB J.* 2008;22(7):2445-51.

51. Kelly PJ, Daumas-Duport C, Kispert DB, Kall BA, Scheithauer BW, Illig JJ. Imaging-based stereotaxic serial biopsies in untreated intracranial glial neoplasms. *J Neurosurg.* 1987;66(6):865-74.
52. Burger PC, Dubois PJ, Schold SC, Jr., Smith KR, Jr., Odom GL, Crafts DC, et al. Computerized tomographic and pathologic studies of the untreated, quiescent, and recurrent glioblastoma multiforme. *J Neurosurg.* 1983;58(2):159-69.
53. Khalil AA, Jameson MJ, Broaddus WC, Lin PS, Dever SM, Golding SE, et al. The Influence of Hypoxia and pH on Bioluminescence Imaging of Luciferase-Transfected Tumor Cells and Xenografts. *Int J Mol Imaging.* 2013;2013:287697.
54. Nishida N, Yano H, Nishida T, Kamura T, Kojiro M. Angiogenesis in cancer. *Vasc Health Risk Manag.* 2006;2(3):213-9.
55. Walsh JC, Lebedev A, Aten E, Madsen K, Marciano L, Kolb HC. The clinical importance of assessing tumor hypoxia: relationship of tumor hypoxia to prognosis and therapeutic opportunities. *Antioxid Redox Signal.* 2014;21(10):1516-54.
56. Amoedo ND, Valencia JP, Rodrigues MF, Galina A, Rumjanek FD. How does the metabolism of tumour cells differ from that of normal cells. *Biosci Rep.* 2013;33(6).
57. Kim MM, Parolia A, Dunphy MP, Venneti S. Non-invasive metabolic imaging of brain tumours in the era of precision medicine. *Nat Rev Clin Oncol.* 2016;13(12):725-39.
58. Horska A, Barker PB. Imaging of brain tumors: MR spectroscopy and metabolic imaging. *Neuroimaging Clin N Am.* 2010;20(3):293-310.
59. Kohler SJ, Yen Y, Wolber J, Chen AP, Albers MJ, Bok R, et al. In vivo ¹³C metabolic imaging at 3T with hyperpolarized ¹³C-1-pyruvate. *Magn Reson Med.* 2007;58(1):65-9.
60. Chaumeil MM, Ozawa T, Park I, Scott K, James CD, Nelson SJ, et al. Hyperpolarized ¹³C MR spectroscopic imaging can be used to monitor Everolimus treatment in vivo in an orthotopic rodent model of glioblastoma. *Neuroimage.* 2012;59(1):193-201.
61. Zhu A, Lee D, Shim H. Metabolic positron emission tomography imaging in cancer detection and therapy response. *Semin Oncol.* 2011;38(1):55-69.
62. Hidalgo M, Amant F, Biankin AV, Budinska E, Byrne AT, Caldas C, et al. Patient-derived xenograft models: an emerging platform for translational cancer research. *Cancer Discov.* 2014;4(9):998-1013.

General Discussion and Conclusions

3 Overview

This thesis highlights the usefulness and importance of using multimodality imaging tools to understand the C6 GBM rat model. Bioluminescence imaging has provided an independent measure of tumour viability to complement tumour burden measurements assessed by mpMRI in this model. GBM is an extremely important disease to understand due to its severity and poor treatment outcomes. The main scientific contributions of this research will be highlighted and summarized below.

3.1 Summary and Conclusions

In this thesis, naïve parental C6 glioma cells were genetically engineered to stably express luciferase and the growth of these cells in an orthotopic rat model was characterized using a multimodality imaging framework that consisted of BLI and mpMRI. One goal of this thesis was to apply this imaging framework to understand how clinically relevant mpMRI measurements of tumour burden may be related to an individual measure of tumour viability assessed with BLI in a longitudinal experiment. A secondary goal of this thesis was to understand BLI and mpMRI imaging parameters of tumour burden/viability during natural progression of C6Luc tumours (*i.e.*, no treatment). This will play an important role in future imaging research involving treated animals because it provides a deeper understanding of how these imaging metrics assess tumour progression in non-treated animals, thus allowing us to properly assess the efficacy of the treatment.

This work began with *in vitro* demonstration that the genetic modification of C6 glioma cells and the BLI substrate, D-Luc, had no significant effect on the proliferation rate of the cells. A linear relationship was observed between cell count and BLI signal intensity *in vitro*, thus it is logical to assume that this linear relationship exists for tumour size and BLI signal intensity *in vivo* (1). Longitudinal *in vivo* experiments showed that there were no significant changes in BLI signal but there were significant increases in post-Gd T_1 - and T_2 MR metrics of tumour volume. The lack of significant changes in BLI could be due in part to the large variation between animals, as animals with the same tumour implantations can develop biologically different tumours from one another, as previously reported (1) and as shown in mpMRI and histology. Correlational analyses showed that post-Gd T_1 and T_2 offered similar metrics of tumour burden and the results provide evidence that the linear relationship between BLI signal intensity and mpMRI tumour burden no longer hold true past day 11 as the two metrics diverge. Upon closer investigation into days 11 to 18, the formation of NCE regions within the tumour were apparent, which was usually surrounded by a region of CE tumour. Post-Gd T_1 -weighted MR images and ADC maps suggest that NCE regions correspond to regions of decreased cellularity. Histology (H&E, DAPI, GFP and hypoxia staining), co-registered with the mpMRI data provided evidence that NCE regions were in fact necrotic, and that among animals, there were varying numbers of viable tumour cells (as determined by GFP). Hypoxia staining showed small hypoxic regions within the tumour, providing qualitative evidence that hypoxia may not have been a large contributing factor to the decrease in BLI signal. These results further suggest that a wide suite of imaging tools is required to fully understand and characterize GBM progression in animal models. BLI, mpMRI and immunohistochemistry has provided insight into the

biology of the tumour and a closer look at biological and morphological features at end-point.

In summary, this is the first study to date to simultaneously apply BLI and mpMRI to characterize the natural progression of C6Luc GBM in rodents and to utilize whole brain histology to qualitatively assess tumour biology and morphology at end-point. The absence of a direct metric for tumour viability with mpMRI has been addressed by adding BLI. This study has shown that BLI offers complementary information to MRI that provides insight into tumour progression, which may have been missed if only the morphological imaging capabilities of mpMRI were used. Whole brain histology has been used to qualitatively assess the tumour at end-point, which suggests that NCE regions in post-Gd T_1 -weighted MR images and regions of increased ADC values correspond to necrosis. From these data, it is highly suggestive and probable that the decrease in tumour viability is a major contributor to the decrease in BLI signal as seen on days 15 and 18.

3.2 Limitations

This section will address some of the major limitations discussed in chapter 2 and in this thesis as a whole, which will be discussed in further detail below.

As discussed in chapter 2, a major limitation of this study was the lack of quantitative longitudinal histology. Histology at each time point (days 4, 8, 11 and 15) would have provided concrete evidence of the various biological and morphological changes occurring within the tumour rather than inference of the processes based on end-point histology. As a result, it is more difficult to draw firm conclusions and correlate the various metrics from

in vivo imaging to the biological and morphological processes apparent in immunohistochemistry at end-point. Although expensive and time-consuming, the ability to correlate the amount of necrosis, or hypoxia to *in vivo* imaging data in a series of longitudinal measurements across numerous animal cohorts would have been ideal, and this absence is a notable limitation of this thesis.

Perfusion imaging data would have provided additional evidence for some of the conclusions and would provide insight into whether the necrotic core was ill-perfused, and had limited substrate delivery. This should be included in future studies involving assessment of therapeutic response of solid tumours.

Having a limited sample size ($n = 11$) made it difficult to conclude any significant trends between different animal tumour growth patterns. There is concern whether each animal should be assessed individually or within a group, due to the large biological variation. It is difficult to draw conclusions regarding observations from individual animals due to the lack of statistical power, but it is apparent that multiple individuals displayed similar growth patterns. With a larger cohort size, it may have been possible to propose that there are patterns of tumour development among animals and subsequently group animals with similar growth patterns depending on observed BLI trends.

Beyond these study specific limitations, the resolution of our mpMR images could be improved. Due to limitations associated with some pulse sequence implementations the maximum performance of the gradient insert was not achieved for this imaging study. Image voxels were limited to an isotropic resolution of 400 μm . Without significant pulse sequence programming effort, it was not feasible to modify these sequences. The sequences

used in this experiment were not optimized to be used with the insertable gradient in research mode. The sequence was hard-coded to prevent a higher resolution.

3.3 Future Directions

The inclusion of multiple modalities into our imaging suite to characterize tumour progression would be a powerful asset. There are multiple clinically relevant imaging modalities, such as PET, and novel imaging modalities, such as HP ^{13}C MRSI, that can directly probe tumour metabolism and provide information about metabolic pathways within tumour cells and inform on the tumour microenvironment. These measurements could be correlated to BLI observations, and would potentially provide a stronger understanding of tumour biology on a molecular level. In addition to metabolic information, contrast agents that probe for hypoxia, vascularization or perfusion would provide a great deal of information regarding the biological microenvironment of the tumour. The ability to employ various PET tracers, such as FMISO to image hypoxia (2), or FDG to image tumour metabolism (3), and various MRI techniques, such as perfusion MRI (4) or HP ^{13}C MRSI to probe metabolism (5), using a hybrid PET/MRI system would provide a great deal of information in addition to BLI, and would be ideal.

The next steps arising from this research would be to take this multimodality imaging framework and apply it to the assessment of treatment response in this model. The results from chapter 2 serve as guide for potential future studies involving novel therapies and the assessment of its efficacy. Inclusion of an independent measure of tumour viability will prove to be invaluable for assessment of the efficacy of novel therapies in addition to morphological changes assessed by MRI, which are slow and lack direct biological and

molecular information. In addition, other cells within the tumour could experience various growth rates due to the tumour microenvironment and the heterogeneity of the tumour, making it difficult to correctly assess treatment response solely on anatomical metrics in MRI. For example, a researcher using only MRI metrics of tumour burden to evaluate C6 tumour growth and response to treatment may make the mistake of assuming that the whole tumour mass consists of viable cells (based on T_2 -weighted images) when this may not be true based on declining BLI measurements that indicate a shrinking viable tumour volume. Likewise, it is important to understand the patterns and trends associated with each specific glioma model and suite of imaging tools. A researcher applying novel therapy on day 11 using both BLI and mpMRI to measure response may make the mistake of misattributing the true cause of the two-fold decrease in BLI signal from day 11 to 15. This researcher would likely conclude that the therapy is efficient in treating GBM without a priori knowledge that progression of this orthotopic C6Luc Wistar rat model often exhibits a significant reduction in BLI beyond day 11.

Clinically relevant animal models such as patient-derived xenograft (PDX) models (6), are of a great interest to the type of work described in this thesis. The use of PDX in a rodent model is extremely useful when considering the evaluation of tumour response to novel therapies as these models more closely recapitulate the biology of human GBM. The observed response from treatment in these models would likely better reflect the expected biological response and efficacy of novel therapies applied in the clinic (7, 8).

3.4 Significance and Impact

GBM is an incurable disease. Current aggressive therapeutic regimens only slow disease progression and temporarily prolong the patient's life. A significant amount of research is aimed towards developing new treatments (9) and methods to better evaluate existing treatments (10). This thesis has shown the utility of a multimodality imaging framework for preclinical GBM research. Multimodality imaging provides important additional information directly related to tumour biology, which complements tumour morphology. BLI has been shown to be a useful tool for measuring tumour viability, and provides unique information in addition to conventional assessment data including tumour volume (T_1 and T_2) and tumour cellularity (ADC). Finally, this thesis has provided caution for future research evaluating novel therapies with imaging without prior comprehensive knowledge of the typical progression of a particular tumour model.

3.5 References

1. Jost SC, Collins L, Travers S, Piwnica-Worms D, Garbow JR. Measuring brain tumor growth: combined bioluminescence imaging-magnetic resonance imaging strategy. *Mol Imaging*. 2009;8(5):245-53.
2. Wang H, Zhang Y, Yu W, Zhao X, Xue Y, Xu H. Radiosensitizing effect of irisinone on glioma through the downregulation of HIF-1alpha evaluated by 18F-FDG and 18F-FMISO PET/CT. *Nucl Med Commun*. 2016;37(7):705-14.
3. Assadian S, Aliaga A, Del Maestro RF, Evans AC, Bedell BJ. FDG-PET imaging for the evaluation of antiglioma agents in a rat model. *Neuro Oncol*. 2008;10(3):292-9.
4. Essock-Burns E, Lupo JM, Cha S, Polley MY, Butowski NA, Chang SM, et al. Assessment of perfusion MRI-derived parameters in evaluating and predicting response to antiangiogenic therapy in patients with newly diagnosed glioblastoma. *Neuro Oncol*. 2011;13(1):119-31.

5. Park JM, Recht LD, Josan S, Merchant M, Jang T, Yen YF, et al. Metabolic response of glioma to dichloroacetate measured in vivo by hyperpolarized (13)C magnetic resonance spectroscopic imaging. *Neuro Oncol.* 2013;15(4):433-41.
6. Lenting K, Verhaak R, Ter Laan M, Wesseling P, Leenders W. Glioma: experimental models and reality. *Acta Neuropathol.* 2017;133(2):263-82.
7. Joo KM, Kim J, Jin J, Kim M, Seol HJ, Muradov J, et al. Patient-specific orthotopic glioblastoma xenograft models recapitulate the histopathology and biology of human glioblastomas in situ. *Cell Rep.* 2013;3(1):260-73.
8. de Jong M, Essers J, van Weerden WM. Imaging preclinical tumour models: improving translational power. *Nat Rev Cancer.* 2014;14(7):481-93.
9. Perry J, Okamoto M, Guiou M, Shirai K, Errett A, Chakravarti A. Novel therapies in glioblastoma. *Neurol Res Int.* 2012;2012:428565.
10. Mabray MC, Barajas RF, Jr., Cha S. Modern brain tumor imaging. *Brain Tumor Res Treat.* 2015;3(1):8-23.

Appendix

Appendix A. Animal Research Ethics Approval



PI :	Scholl, Timothy
Protocol #	2014-040
Status :	Approved (w/o Stipulation)
Approved :	01/23/2015
Expires :	01/01/2019
Title :	Development of Hyperpolarized Metabolic Probes for Magnetic Resonance Imaging of Disease in Animal Models

Table of Contents

- [Animal Use Protocol Overview](#)
- [Funding Source List](#)
- [Purpose of Animal Use](#)
- [Hazardous Materials](#)
- [Animal Movement Between Sites](#)
- [Animal Groups and Experimental Timelines Overview](#)
- [Rat](#)
- [Break](#)
- [Justification for Choice of Species](#)
- [the 3Rs: Replace, Reduce, Refine](#)
- [Species Strains](#)
- [Animal Transfers](#)
- [Environmental Enrichment](#)
- [Animal Holding/Housing and Use Location Information](#)
- [Holding beyond 12 hours](#)
- [Acclimatization Period & Quarantine](#)
- [Experimental Agents Information](#)
- [SOP List](#)
- [Procedures Checklist for Reporting and Training](#)
- [Procedures Narrative](#)
- [Procedural Consequences & Monitoring](#)
- [Endpoint Method Information](#)
- [Animal Numbers Requested](#)
- [Personnel List](#)
- [Protocol Attachments](#)

Protocol Introduction

The questions on this page activate specific sections within the AUP form.

Note that species selection is part of this introductory page

Does this AUP involve teaching?

Yes No

Is the animal work on this project shared by another Animal Care Committee?

Yes No

Will you be using hazards?

Yes No

Will live animals be moved outside of their housing facility?

Yes No

Will field studies be conducted?

Yes No **Add/Update/Remove Species Used on this Protocol**

Species	Agents	Drugs	Restraint	Breeding
Rat	Yes	No	No	

Animal Use Protocol Overview

Animal Use Protocol Title

Development of Hyperpolarized Metabolic Probes for Magnetic Resonance Imaging of Disease in Animal Models

Application Type. If this is a post-pilot project, please attach the Pilot Report to this section, below.

Post-Pilot Full Protocol

Provide Associated Previous Protocol Number

2010-273

Please provide a report detailing the previous AUP's use of Animals

Post Pilot Update.

The pilot AUP (2010-273) helped establish our hyperpolarized metabolic probes research and answer some important associated questions. Within the four years of the pilot protocol:

1) We were able to develop novel dual-frequency RF hardware and compatible animal support hardware for hyperpolarized magnetic resonance imaging using healthy animals. This early research established that the RF hardware had sufficient sensitivity for in vivo experiments. It also established our ability to hyperpolarize endogenous compounds for injection as contrast agents and safely inject them into the tail veins of rats and rapidly image metabolism. We were also able to gauge imaging signal-to-noise ratio which determines the spatial resolution of our metabolic imaging experiments. Our imaging hardware is being used for all hyperpolarized preclinical imaging experiments at Robarts.

2) From early experiments we were able to determine the change in lactate conversion from pyruvate in response to radio- and chemotherapies. This information allows us to calculate accurate cohort numbers for our longitudinal studies.

3) We have observed significant changes in tumour hypoxia using metabolic imaging of hyperpolarized pyruvate as early as two days post therapy. This provides a much earlier assessment than changes in tumour volume measured from MRI or CT.

4) Early experiments using hyperpolarized ¹³C bicarbonate have demonstrated our ability to measure pH in solid tumours.

These experiments have provided useful data for 7 research articles, the renewal of a research grant from the Ontario Institute for Cancer Research, two research grants from Cancer Care Ontario and a funding application to the Canadian Institutes for Health Research, which is still pending.

The 3Rs

Reduction: Our preliminary research has allowed us to refine our surgical techniques and animal care to reduce animal mortality. We also have established animal numbers to power our statistical comparisons between animal cohorts. Our experiments require cohort numbers of approximately eight animals per treatment group to establish significance between groups. We are requesting an additional four animals based on our experiences to date to replace those animals that do not survive to the experimental endpoint (if necessary).

Replacement: We are studying the response of solid tumours to realistic clinical treatment as a first step to eventual clinical translation and as such, we require a realistic tumour model. The C6 rat glioblastoma is an excellent experimental model for our research. The tumours are precisely located through stereotactic intracranial implantation and grow with relative speed and predictability from animal to animal. These tumours have good contrast compared with healthy brain tissue with magnetic resonance imaging. Their location within the skull provides improved tumour location and reduced image artefact from animal motion.

Refinement: We are constantly improving our experimental apparatus and imaging methods with an aim to improved

imaging results. This will decrease the number of animals required for our studies. We are also developing new formulations for hyperpolarized probes, which will produce improved imaging results with decreased injected dose.

Using non-scientific language, please describe the project's purpose, expected benefit, and a brief summary of your work with the animal model(s).

Please be aware that in the event of communications with Western Media Relations and the PI is not available, this summary will be sent to Western Media Relations.

Molecular imaging is a rapidly developing field, which non-invasively visualizes cellular function such as metabolism. Our research has focused on development of novel molecular imaging probes for magnetic resonance imaging (MRI) with a specific emphasis on application to cancer imaging. Therapeutic choice for an individual cancer patient relies on invasive tumour sampling. For many targeted agents, molecular assessment is particularly important to both apply these agents to cancers that are most likely to respond and avoid treatments that are unlikely to be effective. Sadly, predictive biomarkers are not perfect prognosticators of therapeutic response or failure for a given agent in a particular patient and treatment assessment often relies on longitudinal measurements of changes in tumour size. Significant changes in tumour size can take months to become apparent if at all. Molecular imaging has the potential to non-invasively assess subtle changes in disease. For cancer, it can assess the evolution of the tumour microenvironment, determine the potential for tumour proliferation and, perhaps most importantly, provide prompt evidence for early responses versus non-responses during ongoing treatment.

Since MRI is a valuable diagnostic imaging tool capable of morphological and functional imaging with high spatial resolution and is the standard of care for assessment of most solid tumours, the added capability to assess molecular function is an important development, particularly for cancer research. For example, our preclinical research is demonstrating the ability to measure metabolic changes in the tumour such as hypoxia as soon as one day after initiation of therapy. This research using hyperpolarized metabolic imaging of hyperpolarized ^{13}C -enriched compounds has produced seven peer-reviewed research articles and 17 conference abstracts over the past four years. In addition, a recent oral presentation of one of my PhD student's thesis entitled "Molecular imaging of tumor metabolism: a longitudinal study of tumour response to therapies using hyperpolarized ^{13}C pyruvate" received a Magna Cum Laude Merit Award (top 5%) at the 2014 Scientific Meeting of the International Society for Magnetic Resonance in Medicine in Milan, Italy.

The next steps for our hyperpolarized imaging research is to investigate additional probes of the tumour microenvironment. Our initial experiments have focused on pyruvate metabolism and its role in assessing hypoxia. We are currently interesting in assessing changes in pH, which tumours exploit for proliferative advantage. Using hyperpolarized ^{13}C bicarbonate, we plan to non-invasively measure extracellular pH and compare that with the intracellular pH assessed through chemical exchange saturation transfer (CEST) magnetic resonance imaging in tumour cells. Cellular necrosis in response to therapy can also be measured through conversion of hyperpolarized fumarate to malate as cellular walls break down. These three important biomarkers of the tumour microenvironment (hypoxia, pH and cellular necrosis) will be studied simultaneously in a rat model of glioma to look at their prognostic potential for early assessment of treatment response and longer term treatment outcome in extended longitudinal studies.

We are working with John Ronald to modify our brain cancer cell line for in vivo animal experiments. We have engineered these cells so that they produce a fluorescent green protein which makes the viable tumour cells much more visible under histology. In addition, the cells produce an enzyme known as luciferase, which can be used for bioluminescence imaging (BLI). Our animals are injected with a small amount of a compound known as luciferin. The luciferase produced by living tumour cells cause a chemical reaction with the luciferin that produces light. The amount of light that we measure with BLI is proportional to the number of living tumour cells. This allows us to non-invasively measure tumour burden in longitudinal studies of therapy. This is our gold-standard against which we can compare our other methods such as metabolic imaging of pyruvate, measurements of pH and cellular necrosis.

GLOSSARY OF TERMS - Identify each individual scientific term and abbreviation using CAPITAL LETTERS, and then briefly define each term to be referenced in any section of this protocol.

e.g. ALLELE - The genetic variant of a gene responsible for the different traits of certain characteristics and genetic diseases.

MRI - Magnetic Resonance Imaging.

^{13}C - A naturally occurring non-radioactive isotope of carbon (1.11% natural abundance).

HYPERPOLARIZATION - A technique for enhancing MRI signal strength by factors of up to 100,000.

PYRUVATE - An endogenous intermediate in carbohydrate metabolism.

BICARBONATE - An endogenous compound used to measure in vivo pH with hyperpolarized imaging.

CEST - Chemical exchange saturation transfer. This is a magnetic resonance imaging technique that is used to measure intracellular pH. This is a non-invasive imaging method that does not require injection of a contrast agent.

GLIOBLASTOMA or GLIOMA - A glioma is a type of tumor that starts in the brain or spine, more specifically the definition of glioma is a primary brain tumor that originates from the supportive cells of the brain, called glial cells. Glial cells are the most common cellular component of the brain. There are five to ten times more glial cells than neurons. A Glioblastoma is a

particular type of Glioma (Astrocytoma).

FUMARATE - An endogenous intermediate in the citric acid cycle (krebs cycle).

MOLECULAR IMAGING - a non-invasive means to visualize cellular function such as metabolism.

BLI - Bioluminescence imaging is a means of measuring the biodistribution of cells that have been engineered to produce light after injection of a contrast agent.

Luciferin -is a light-emitting compound which is injected into animals to generate bioluminescence. Cells in these animals, which produce the enzyme luciferase cause a chemical reaction with luciferin producing light that can be imaged by BLI.

Here is the link to CCAC's Policy on Scientific Merit and Ethical Review of Animal-based Research:

http://www.ccac.ca/Documents/Standards/Policies/Scientific_merit_and_ethical_review_of_animal-based_research.pdf
(http://www.ccac.ca/Documents/Standards/Policies/Scientific_merit_and_ethical_review_of_animal-based_research.pdf)

Has the work outlined in this AUP received favourable scientific peer review?

Yes No

Do you wish to provide a funding peer review assessment, which may be considered in lieu of internal scientific peer review? If 'YES', please attach the funding assessment.

Yes No

If this is a RESEARCH AUP, please provide a list of one to three publications relevant to the work outlined in this AUP.

If this is a resarch AUP, attach an OUTLINE for scientific merit reviewers that provides sufficient information that another scientist working in the same field of study could effectively review this AUP's scientific merit, below. PIs may utilize whichever format best describes its scientific merit, e.g. background, rationale, hypothesis, objectives, experimental procedures

Using only key words, specify the animal models and procedures described within this AUP.

Research/ Anesthesia/ Imaging/ Stereotaxic Surgery/ Tumour Cell Injections/ Analgesia/ Chemotherapy/ Injection IP/
Radiotherapy/ Euthanasia

Curriculum Vitae

- Name:** Trung N.T. Le
- Post-secondary Education and Degrees:**
- Masters of Science Candidate**
 Medical Biophysics (Molecular Imaging)
 University of Western Ontario
 London, Ontario, Canada
 2015-2017
- Bachelors of Science**
 Honors (Major in Biology and Medical Science)
 University of Western Ontario
 London, Ontario, Canada
 2010-2015
- Honours and Awards:**
- Western Graduate Research Scholarship**
 Department of Medical Biophysics. University of Western Ontario
 \$1,500 per term
 2015-2017
- Related Work Experience:**
- Graduate Research Assistant**
 Robarts Research Institute
 London, Ontario, Canada
 Department of Medical Biophysics. University of Western Ontario
Supervisors: Drs. Timothy J. Scholl and John A. Ronald
 2015 – Present
- Publications and presentations:**
- Publications (1)**
- TNT Le, H Lim, A Hamilton, KM Parkins, FM Martinez, TJ Scholl, and JA Ronald.** Multiparametric Magnetic Resonance Imaging and Bioluminescence Imaging Characterization of an Orthotopic Rat Model of Glioblastoma. *In preparation.*
- Presentations (6)**
- TNT Le, H Lim, A Hamilton, KM Parkins, FM Martinez, TJ Scholl, and JA Ronald.** Characterizing the Orthotopic C6 Glioblastoma Rat Model with Multiparametric Magnetic Resonance Imaging and Bioluminescence Imaging. Oral presentation. Imaging Network of Ontario, Toronto, Ontario. 2017

- Publications and presentations:** **TNT Le, H Lim, A Hamilton, FM Martinez, KM Parkins, TJ Scholl, JA Ronald, Characterizing the Orthotopic C6 Glioblastoma Rat Model with Multiparametric Magnetic Resonance Imaging and Bioluminescence Imaging. Poster presentation. London Health Research Day, London, Ontario. 2017**
- TNT Le, H Lim, A Hamilton, FM Martinez, KM Parkins, TJ Scholl and JA Ronald. Imaging Tumour Metabolism Using Novel Multi-Modality Molecular Imaging in an Orthotopic Rat Model of Glioblastoma Multiforme. Poster presentation. World Molecular Imaging Congress. New York City, New York. September 2016.**
- TNT Le, H Lim, A Hamilton, FM Martinez, KM Parkins, TJ Scholl and JA Ronald. Towards Evaluating Treatment Response of Glioma in a Rat Model Using Novel Multi-Modality Imaging. Oral presentation. Robarts Retreat. London, Ontario. June 2016.**
- TNT Le, H Lim, A Hamilton, FM Martinez, KM Parkins, TJ Scholl and JA Ronald. Towards Assessing Therapeutic Response of Glioblastoma Multiforme Using Novel Multi-Modality Imaging. Poster presentation. Imaging Network of Ontario. London, Ontario. March 2016.**
- TNT Le, H Lim, A Hamilton, FM Martinez, KM Parkins, TJ Scholl and JA Ronald. Towards Assessing Therapeutic Response of Glioblastoma Multiforme Using Novel Multi-Modality Imaging. Poster presentation. London Health Research Day. London, Ontario. March 2016.**